POLITECNICO DI TORINO

Master of Science

in Mechanical Engineering

Master's Thesis

Surrogate Fuel Definition And Spray Calibration For Diesel Engines

Supervisors

Prof. Mirko Baratta

Prof. Daniela A. Misul

Candidate

Stefano Lanfaloni

July 2020

Abstract

Reducing the greenhouse gas emissions is one of the most important targets in the automotive industry and to do so, a shift to carbon-neutral fuels is one of the most promising alternatives. Due to their composition, hydrotreated vegetable oils (HVOs) are very high quality bio-based diesel fuels, with no negative effects on engines or exhaust after treatment system. In partnership with ENI, a research activity at the Energy Department in Politecnico di Torino has been started to investigate the effects of using HVO instead of a conventional diesel fuel. The first step has been the development of a CFD model of a light-duty commercial vehicle equipped with a compression-ignition engine powered with conventional diesel fuel. In the present thesis, as next step, a surrogate fuel approach to simulate the HVO has been developed and the spray CFD model has been calibrated. Numerical results are validated against experimental data, available on the ECN platform, in terms of liquid and vapor penetration, ignition delay and location, lift-off length and soot mass formation. First part of this thesis will serve as an introduction, describing the hydrotreated vegetable oil and the ENI project. Moreover a theoretical background on CFD fundamentals and the CONVERGE CFD software is provided. The second part deals with the development of the fuel surrogate approach. In the third part the spray model using the surrogate fuels is calibrated and results are validated against the experimental data. In the fourth part, finally, the next steps and the possible future implementations will be discussed.

CONTENTS

1 INTRODUCTION

1.1 Present situation

As climate change and air pollution have become problems that require active and immediate actions to solve or, with a realistic position, at least reduce, the automotive industry has start to push towards innovative solutions in terms of engine and after treatment systems efficiency. Since the available technology to improve engine efficiency (which results in lower fuel consumption and thus in lower emissions) is reaching its limits, also the fuel industry has started to develop and propose new types of combustibles. The aim is to maintain the performance but at the same time, using fuels that will result in lower emissions. One of the most promising solution appeared to be the bio-fuels: the carbon dioxide emitted during their production processes and combustion in automotive applications, is compensated by the amount of CO_2 absorbed during the life-cycle of the biomasses from which bio-fuels derive which are therefore considered as carbon-neutral.

Bio-fuels represent a promising solution that will allow not only to tackle the greenhouse gases emission but also maintain, or even increase, the engine performance: the Bentley Continental Supersport and the Koenigsegg Gemera, for example, can be fueled with bio-ethanol and even increase their performance.

Since compression ignition diesel fueled engines usually present higher efficiency thanks to higher compression ratio and higher volumetric efficiency (absence of throttling valve), the development of bio-based diesel fuels is an interesting and promising solution.

1.2 Hydrotreated Vegetable Oil (HVO)

Traditional bio-diesels are generally produced by transesterification reactions with methanol, resulting in a main composition of saturated and unsaturated methyl esters with long alkyl chains[1]. These biodiesels are the so-called FAME (Fatty Acid Methyl Esters): main drawback is the presence of oxygenated compounds that will result in a less reactive fuel and will require an adjustment in the engine calibration. Moreover the NO_x emissions increase and, if used pure, it will cause deposit formation and therefore reduce the life of the engine.

Hydroteated vegetable oil also derives from bio-masses but the process is different. The plants oil, triglycerides, are subjected to hydrogenolysis, a process where hydrogen is used to break the single carbon-heteroatom bond in order to remove the oxygen: the products of this process are alkanes which then undergo to a catalytic isomerization in order to increase the number of branched (iso-) alkanes: this is done to meet the required cloud point for commercial fuels. The hydrogenolysis is a process that is also used in petroleum refinement plants to reduce the sulfur content to a neglectable quantity.

Resulting fuel is a high-quality bio-based diesel, composed only of paraffins (both linear and branched) with a cetane number higher than the traditional diesel, a lower density and distillation curve that can be used without concerns on engine performance or duration reductions.

-insert refs, tables with values and distillation curve-

The Fischer-Tropsch (FT) process, based on alkanes production starting from carbon dioxide and hydrogen, can be used to produce a similar fuel, with an only-alkanes composition: however, the only commercial available FT fuels are refined from fossil sources. Fischer-Tropsch process is, in fact, getting intermittent attention since it can be used to reduce the costs in fuel production and produce directly low-sulfur fuels.

1.3 The ENI project

The growing attention on carbon-neutral fuels has stimulated the interest of some oil companies with a focus on fighting the climate-change and the pollutant emissions. One of them is the Italian company ENI S.p.A. that has recently started a research activity with the cooperation of the Energetic Department of Politecnico di Torino in order to investigate the potential and the possible applications of the HVO produced by them.

As said, FAME could cause different problems such as particulate filter clogging and increased NO_x emissions: the European regulation about automotive diesel, therefore, has defined a limit of 7% in volume for the FAME content in commercialized diesel. On the contrary, hydrotreated vegetable oil can be used pure without the risk of damaging the engine or the after treatment system, so HVO can be commercialized both pure or mixed, in high percentages, with traditional diesel: the only limitation is to meet the properties imposed by the UNI EN 590 regulation.

The objective of the project is to investigate the performance and the emissions deriving from fueling new generation compression-ignition engines with pure HVO pure or traditional diesel with a high content of it: this will lead to an optimization of the fuel for both conventional compression-ignition engines and for those developed to be fueled specifically with HVO.

The investigation will be done on a light duty commercial compression-ignition engine (insert F1A engine specs): a 3D-CFD (three-dimensional computational fluid dynamics) model will be developed, using the work of a previous master thesis [2] as a starting point, and validated against experimental data obtained testing the engine fueled with conventional diesel and HVO. Thus the research activity group will be also able to compare the variations in terms of performance and emissions deriving from switching to the bio-diesel.

Objective of this thesis is the definition of a surrogate fuel approach to simulate both conventional diesel and hydrotreated vegetable oil. The resulting fuels will be then be implemented in numerical model of spray injection that will be calibrated and validated against experimental data available on the Engine Combustion Network (ECN) platform. It should be noticed that calibrating the spray injection model is a fundamental step in the development of the diesel engine combustion modelling.

2 COMPUTATIONAL FLUID DYNAMICS

2.1 Introduction

Flows and related phenomena can be described by partial differential (or integro-differential) equations, which can be solved analytically only in special cases. An approximate numerical solution is obtained using a discretization method which approximates the differential equations by a system of algebraic equations, which can then be solved on a computer. The approximations are applied to small domains in space and/or time so the numerical solution provides results at discrete locations in space and time [3]. This application of numerical methods to solve and analyze problems related to fluid flows is, in essence, what is called computational fluid dynamics (CFD).

CFD is the most sophisticated approach for detailed numerical investigations on thermo-fluid dynamical problems. In other words, it is a tool to perform numerical simulations, as physical experiments are usually too complicated, or too expensive to be done.

CFD has become a fundamental tool in the automotive industry since the results obtained from numerical engine simulations make possible the most detailed physical description of the relevant processes.

However, different conditions are necessary to obtain results representative of real phenomena using CFD: (1) appropriate discretization of the flow domain (mesh generation), able to properly capture relevant physical processes; (2) correct boundary and initial conditions, such as pressures, temperatures, turbulence parameters, and other; (3) calibration of the numerical models used for simulation of various processes (spray, combustion, turbulence, etc.) using experimental data, experience available from past simulations or available in literature.

Finally, it should be noted that CFD is typically a computationally expensive process, requiring high processing power to perform a simulation in an acceptable time. Moreover, many simulations are required to investigate the influence of different parameters on the engine performance. Therefore a trade-off between computational load and accuracy has to be found: in fact an excess of the first leads to longer development time, while a lack of the second will produce useless results.

2.2 Governing equations

CFD is based on the fundamental equations of fluid dynamics: continuity, momentum, and energy equations. These are the mathematical representation of the following three physical principles:

1) Mass is conserved.
2) Newton’s second law, $\vec{F} = m\vec{a}$
3) Energy is conserved.

Governing equations can be obtained in different forms (integral or partial differential, conservative or non-conservative), depending on which flow model they are applied to. The flowchart in Fig.1 reports the process of obtaining these equations.

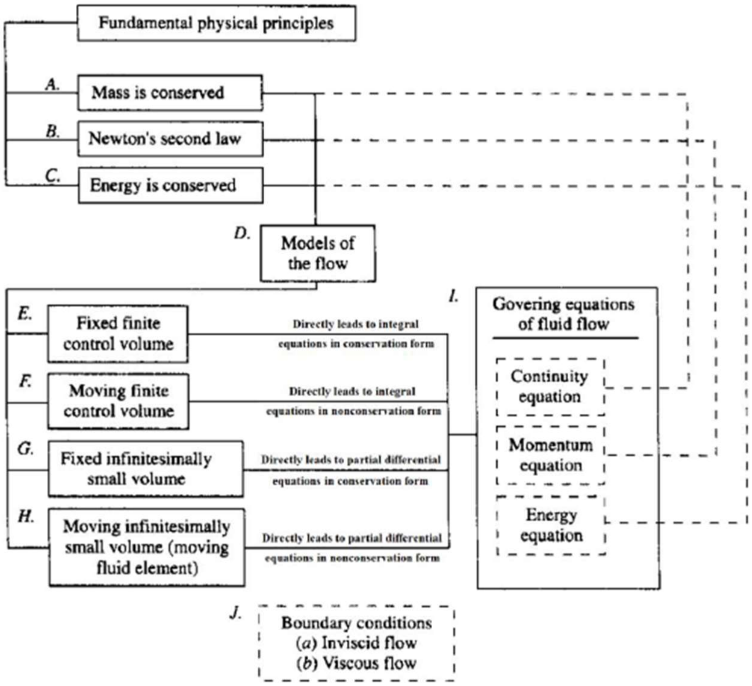

Fig. 1

It can be noticed that there are four different models of the flow, each producing a different mathematical statement of the governing equations:

1) Fixed finite control volume (Fig.2a, left): the control volume V is fixed in space with the fluid moving through it. Integral equations in conservation form are obtained.
2) Moving finite control volume (Fig.2a, right): the control volume V is moving with the fluid such that the same fluid particles are always inside it. Integral equations in non-conservation form are obtained.
3) Fixed infinitesimally small volume (Fig.2b, left), where the differential volume dV is fixed in space with the fluid moving through it. Partial differential equations in conservation form are obtained.
4) Moving infinitesimally small volume (Fig.2b, right), where the differential volume dV moves along a streamline. Partial differential equations in non-conservation form are obtained.

Control volume V is a reasonably large and finite flow region, while differential volume dV is a region large enough to contain a huge number of molecules.

The results obtained from these methods are affected significantly by the adopted grid: in the limit case of a very fine grid, in fact, each method produce the same results, while using a coarse grid the non-conservative form introduces additional approximations that can be significant [3].

The governing equations must be solved subject to the physical boundary conditions. As the physical aspects of the boundary conditions are fundamentally independent of the forms of the governing equations, the box representing the boundary conditions stands by itself at the bottom of Fig.1, unconnected to any of the other boxes in the flowchart [4].

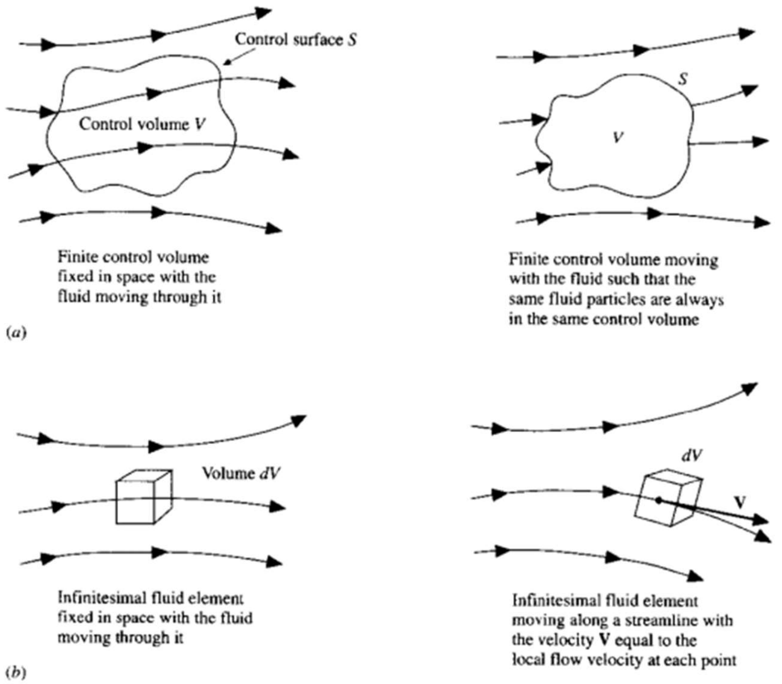

Fig. 2

It is common to refer to the entire system of equations in differential form composed of conservations of mass, momentum, and energy as the Navier-Stokes equations [5]: in fact both of them, independently, derived the conservation of linear momentum in derivative form.

In fluid flows, however, it is difficult to follow a parcel of matter (an infinitesimally small volume) and it is more convenient to deal with the flow within a control volume: this method of analysis is called the control volume approach [3].

2.2.1 Continuity equation

It's the equation deriving from the mass conservation. Applied to the finite control volume fixed in space this means that net mass flow out of control volume through surface S is equal to time rate of decrease of mass inside control volume. Thus an integral form of the continuity equation in conservation form is obtained as:

$$\frac{\partial}{\partial t}\int_{v} \rho dv + \int_{S} \rho\vec{V}\cdot\vec{n}dS = 0$$

Where v is the control volume, S is the surface that enclosure the control volume, $\vec{n}$ is the orthogonal vector to S and $\vec{V}$ is the fluid velocity.

Considering an infinitesimally small fluid element fixed in space (Fig.2b, left) the continuity equation can be rewritten in its partial differential conservative form:

$$\frac{\partial\rho}{\partial t} + \nabla\cdot\left(\rho\vec{V}\right) = 0$$

Where $\nabla\cdot\left(\rho\vec{V}\right)$ is the divergence of the density times velocity.

2.2.2 Momentum equation

The momentum equation is based on Newton's second law, $\vec{F} = m\vec{a}$. Applied to the fluid element, means that the net force on the fluid element equals its mass times the acceleration of the element. There are two sources of this force [4]:

1) Body forces, which act directly on the volumetric mass of the fluid element, such as gravitational, electric and magnetic forces.
2) Surface forces, which act directly on the surface of the fluid element due to the outside fluid surrounding it. They are due to only two sources: pressure distribution and shear and normal stress distributions (friction)

The surface forces due to pressure and stresses can be considered as microscopic momentum fluxes across a surface. If these fluxes can't be written in terms of the properties whose conservation the equations govern (density and velocity), the system of equations is not closed; that is there are fewer equations than dependent variables and solution is not possible [3]. This can be avoided by considering the fluid as Newtonian and therefore the shear stress is proportional to the time rate of strain, i.e., velocity gradients: fortunately, most of the fluids can be considered as Newtonians fluids.

An integral form of the momentum equation in conservation form (obtained for a finite control volume fixed in space, Fig.2a left) is obtained as:

$$\frac{\partial \rho}{\partial t}\int \rho\vec{V}dv + \int \rho\vec{V}\vec{V}\cdot\vec{n}dS = \int \vec{T}\cdot\vec{n}dS + \int \rho\vec{b}dv$$

Where v is the control volume, S the surface that enclosure the control volume, $\vec{n}$ the orthogonal vector to S, $\vec{V}$ the fluid velocity, $\vec{T}$ the stress tensor and $\vec{b}$ the body forces (per unit mass).

This equation means that the sum of the forces acting on a control volume is equal to the sum of the rate of change of linear momentum within the control volume and net efflux of the linear momentum across the control surfaces [5].

The stress tensor $\vec{T}$ can be written as:

$$\vec{T} = -\left(p + \frac{2}{3}\mu\nabla\cdot\vec{V}\right)\cdot I + 2\mu D$$

Where p is the static pressure, µ dynamic viscosity, I the unit tensor and D the rate of strain tensor:

$$D = \frac{1}{2}\left[\nabla\vec{V} + \left(\nabla\vec{V}\right)^T\right]$$

The continuity equation in partial differential form is the Navier-Stokes equation and is written as:

$$\frac{\partial(\rho\vec{V})}{\partial t} + \nabla\cdot\left(\rho\vec{V}\vec{V}\right) = \nabla\cdot\vec{T} + \rho\vec{b}$$

2.2.3 Energy equation

This equation is based on the energy conservation principle and can be expressed as:

$$\frac{d(\rho e_t)}{dt} = \frac{\partial Q}{\partial t} + \frac{\partial W}{\partial t}$$

Where e_t is the total energy per unit mass, $\frac{\partial Q}{\partial t}$ the heat transfer rate to the system and $\frac{\partial W}{\partial t}$ the rate of the work done on the system.

The total energy e_t can be expressed as the sum of internal energy (e), kinetic energy ($\frac{1}{2}V^2$) and potential energy (gZ):

$$e_t = e + \frac{1}{2}V^2 + gZ$$

2.2.4 State equation

This equation determines the existing relation between the thermodynamic properties of the fluid.

Considering five conservation equations (the continuity equation, the three momentum equations, and the energy equation), there are seven unknowns ρ, p, e, T, u, v, w: additional relations, like the state equation, are required to close the equation system.

In thermodynamics, the state of a fluid is defined by two independent state variables, provided that the chemical composition of the fluid is not changing owing to diffusion or finite-rate chemical reactions.

In most of gas dynamics applications, it’s possible to assume a perfect gas and therefore the following equation:

$$p = \rho RT = \rho \frac{\mathcal{R}}{M} \mathrm{T}$$

Where R is the gas constant, defined as $\mathcal{R}$, the universal gas constant, divided by the molecular weight M.

Moreover, for a perfect gas the internal energy, e, is function only of the temperature:

$$e = e(T)$$

With these two state equation, then, the conservation equations system has the same number of equations and variables and therefore can be solved.

2.3 Discretization

Many approaches are available, but the most important of which are: finite difference (FD), finite volume (FV) and finite element (FE) methods. Each type of method yields the same solution if the grid is very fine. However, some methods are more suitable to some classes of problems than others [3].

2.3.1 Finite Difference Method

The starting point is the conservation equation in differential form. The solution domain is covered by a grid. At each grid point, the differential equation is approximated by replacing the partial derivatives by approximations in terms of the nodal values of the functions. As result, one algebraic equation per grid node is obtained.

Approximations to the first and second derivatives of the variables with respect to the coordinates are obtained using Taylor series expansion or polynomial fitting. When necessary, these methods are also used to obtain variable values at locations other than grid nodes (interpolation).

This method is relatively simple to use for simple geometries, but the conservation is not enforced unless particular conditions are imposed. Moreover, in case of complex flows the restriction to simple geometries becomes a significant disadvantage [3].

2.3.2 Finite Volume Method

Starting point of this method is the integral form of conservation equations . The solution domain is subdivided into a finite number of contiguous control volumes (CVs), and the conservation equations are applied to each CV. Variable values are calculated at the centroid of each CV, where there is a computational node. Interpolation is used to express variable values at the CV surface in terms of the nodal (CV-center) values. Surface and volume integrals are approximated using suitable quadrature formulae. In this case an algebraic equation for each CV, in which a number of neighbor nodal values appear is obtained.

As the grid defines only the control volume boundaries and need not be related to a coordinate system, the FV method is suitable for complex geometries. Another advantage of the finite-volume method is that solving the integral forms of governing equations, mass, momentum, and energy are automatically conserved.

On the other hand, compared to FD method, the FV method has a more complex development in 3D since it is of order higher than second. This is due to the fact that the FV approach requires three levels of approximation: interpolation, differentiation, and integration [3].

The diffusion of the FV method in CFD derives from the high flexibility it offers as a discretization method. In fact the discretization is carried out directly in the physical space with no need for any transformation between the physical and the computational coordinate system [6].

2.3.3 Finite Element Method

This method is similar to the FV one in many ways: i.e., the domain is also broken into a set of discrete volumes or finite elements. Distinguishing feature of FE methods is that the equations are multiplied by a weight function before they are integrated over the entire domain. In the simplest FE methods, the solution is approximated by a linear shape function within each element in a way that guarantees continuity of the solution across element boundaries. Such a function can be constructed from its values at the corners of the elements.

This approximation is then substituted into the weighted integral of the conservation law and the equations to be solved are derived by requiring the derivative of the integral with respect to each nodal value to be zero. The result is a set of non-linear algebraic equations.

Advantages of finite element methods are the ability to deal with arbitrary geometries, easily refined grids and the simple subdivision of each element. The principal drawback is that finding the most efficient solution method is complex since the matrices of the linearized equations are not as well structured as those for regular grids [3].

2.4 Turbulence modeling

Most of engineering applications in fluids involves turbulence: a turbulent flow may be defined as a flow which contains self-sustaining fluctuations of flow properties imposed on the main flow. It is highly unsteady, three-dimensional and contains a great deal of vorticity. Many factors can cause the transition from laminar to turbulent flow. The fundamental quantity describing this transition is the Reynolds number:

$$Re = \frac{\rho V L}{\mu}$$

Where ρ is the fluid density, μ fluid dynamic viscosity, V the flow velocity and L the characteristic linear dimension.

Transition to turbulent flow is influenced by numerous factors like freestream turbulence, pressure gradient, heat transfer, surface roughness, and surface curvature [5]. In the past, an experimental approach was used to study turbulent flows. Overall parameters such as the time-averaged drag or heat transfer are relatively easy to measure but as the sophistication of engineering devices has increased, the levels of detail and accuracy required has also increased, and therefore the cost and difficulty of making measurements. Optimization of a design usually starts with the analysis of undesired effects: this requires detailed measurements that are costly, time-consuming and sometimes almost impossible to make. As a result, again, numerical methods have an important role to play [3].

Numerical solving of the conservation equations in differential form (the Navier-Stokes equations) can be used to predict transition and evolution of turbulence. In fact, this equation system can be numerically solved for any turbulent flow and it is common referred to as Direct Numerical Simulation (DNS). However, this approach requires massive computational power (as all scales of turbulence from smallest to largest must be accommodated) and thus is impractical for most engineering applications due to complex geometry and high Reynolds number flows (with a high number of turbulent scales that have to be resolved) [3].

Another approach is the Large Eddy Simulation (LES), where only the large scale structure in the flow are directly simulated, while small scales are filtered out and computed by turbulence models called sub-grid scale models: the small scale eddies, in fact, are more uniform and have more or less common characteristics. Therefore, these small scale turbulence is modeled and directly resolved. From numerical point of view (compared with DNS), since the small-scale turbulence is now modeled, the grid spacing could be much larger than Kolmogorov length scale (the smallest scale required to describe the turbulent flow). This in turn allows applications of LES to larger Reynolds numbers possible [5]. As a result, LES requires significantly less computational effort and is more applicable for practical purposes.

Third approach is based on equations obtained by averaging the equations of motion over time (if the flow is statistically steady), over a coordinate in which the mean flow does not vary, or over an ensemble of realizations. Thus all of the unsteadiness is averaged out, i.e. all unsteadiness is regarded as part of the turbulence. This approach leads to a set of partial differential equations called the Reynolds-averaged Navier-Stokes (or RANS) equations. These equations do not form a closed set, therefore turbulence models, introducing approximations, are required [3]. Due to the complexity of turbulence, however, these models should only be considered for engineering applications, where the focus is usually on knowing just few quantitative properties of the turbulent flow (average body forces or average mixing degree between two streams). DNS or LES methods require a humongous computational power and the results present a detail level which is not required: therefore direct turbulent resolution methods should be used only in exceptional cases or to validate uncertain RANS results[3].

Fig.3 reports the schematic representation of the turbulent kinetic energy spectrum as a function of the wavenumber k (inverse of the eddy size) and the different possible applications of the tree numerical approaches described.

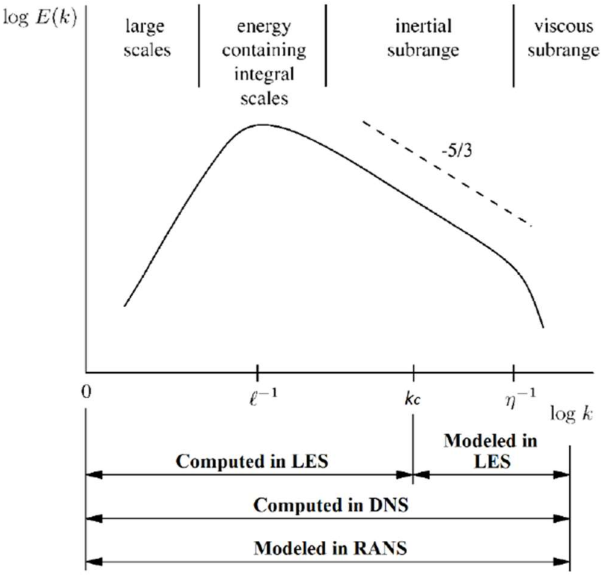

Fig. 3

3 CONVERGE CFD

CONVERGE CFD software is a product of Convergent Science, founded in 1997 and a CFD consulting company in its early years. In 2008, the first CONVERGE licenses were sold and the company transitioned to a CFD software company [8].

CONVERGE software is an advanced CFD tool, especially suited to internal combustion engine simulations. It offers autonomous meshing: the software automatically creates the mesh at runtime, dynamically adapts it throughout the simulation and invokes Adaptive Mesh Refinement to maximize both accuracy and computational efficiency. Moreover, CONVERGE software proposes a wide variety of modeling options for combustion, emissions, spray and turbulence which have been verified and tested for a large number of applications.

The software implements a finite volumes (FV) discretization method.

In Fig.4 the order of equation solving in CONVERGE is reported:

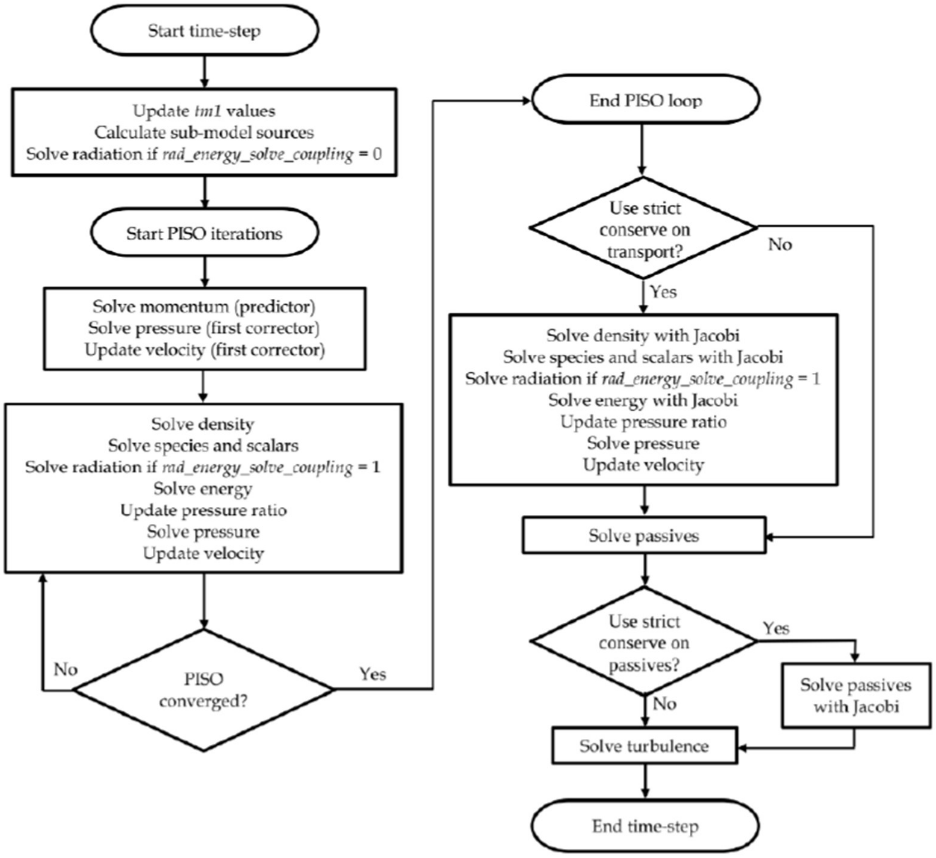

Fig. 4

At the start of each time-step, the previous values [the time-step minus 1 (*tm1* in Fig.4)] are stored for all transported quantities. Then, explicit sources are calculated for each sub-model that is currently activated and radiation is solved if energy and radiation are decoupled. At the beginning of the PISO loop (i.e., the first PISO iteration), CONVERGE solves for momentum and pressure, which sets the velocity for the other transport equations. After each PISO iteration, it is necessary to check for PISO loop convergence. For compressible cases, CONVERGE considers the PISO loop to be converged if [7] $\Delta\rho < piso\_tol$ [7], where $\Delta\rho$ is the density correction and $piso\_tol$ is the PISO tolerance. For incompressible cases, the PISO loop convergence parameter is $\Delta P < piso\_tol$ where ΔP is the pressure correction. If the PISO iteration has converged but the PISO iteration number is less than piso_itmin (which can be user defined), the PISO iterations will continue until the minimum number of PISO iterations has been exceeded. If the PISO iteration did not converge, CONVERGE executes an additional PISO iteration. After the PISO loop has ended, CONVERGE may perform an additional Jacobi iteration to enforce strict conservation. The Jacobi iteration guarantees that the quantity is conserved to machine zero, rather than to the tolerance set by piso_tol. The turbulence equations are outside of the PISO loop for efficiency reasons.

3.1 PISO Algorithm

The pressure-velocity coupling in CONVERGE is achieved using a modified Pressure Implicit with Splitting of Operators (PISO) method, thoroughly explained in [9]. PISO is described as a non-iterative method for handling the coupling of the implicitly discretized time-dependent fluid flow equations.

The method is based on the use of pressure and velocity as dependent variables and thus can be applied to both the compressible and incompressible versions of the transport equations. The main feature of the technique is the splitting of the solution process into a series of steps whereby operations on pressure are decoupled from those on velocity at each step, with the split sets of equations being amenable to solution by standard techniques. At each time-step, the procedure yields solutions which approximate the exact solution of the difference equations [9].

The PISO algorithm as implemented in CONVERGE starts with a predictor step where the momentum equation is solved. After the predictor, a pressure equation is derived and solved, which leads to a correction applied to the momentum equation.

This process of correcting the momentum equation and re-solving can be repeated as many times as necessary to achieve the desired accuracy. After the momentum predictor and first corrector step have been completed, the other transport equations are solved in series [7].

In order to limit the PISO corrections, the minimum and maximum number of PISO corrections allowed can be entered. If the maximum number of PISO iterations is exceeded and the solution has not converged, the following time-step will be reduced.

3.2 Mesh generation

CONVERGE discretizes the domain into control volumes called nodes or cells (terms “node” and “cell” are used interchangeably). Each node is defined by its center and the faces that bound the node. The software uses internal data structures to define the domain(s) of the mesh, assign an order to nodes and the faces of the node, and establish connectivity between nodes.

CONVERGE has an innovative approach to grid generation – it automatically generates the grid at runtime. To make this possible, the software uses a modified cut-cell Cartesian grid generation method. The geometry surface is immersed within a Cartesian block. Cells are trimmed at the intersecting surface, after which the intersection information (surface areas, normal vectors, etc.) is reduced before being stored for each cell. This allows for complex surface intersections to be represented more easily. Cut-cell is shown in Fig.5a.

A slave node is a cut-cell whose volume is less than 30% of the master node volume. In a process called cell pairing, CONVERGE pairs the master and slave nodes to form a single node, which is known as a paired node. The center of the paired node is at the volumetric center of the combined nodes. The master node and the slave node share values of transport entities [7]. Master and slave nodes ae shown in Fig.5b.

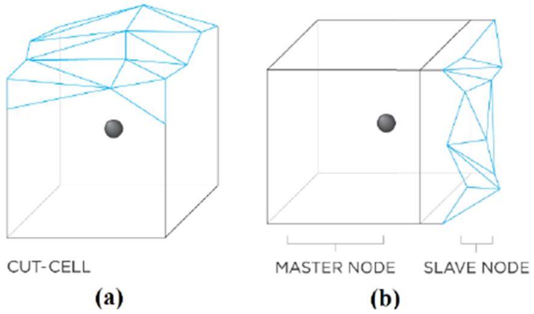

Fig. 5

All nodes are transport nodes (Fig.6a). CONVERGE solves transport entities such as velocity, temperature, and species at the center of a transport node. A parcel cell (also known as a parcel), shown in Fig.6b, is a theoretical representation of spray drops that are identical to one another (i.e., the drops have the same radii, temperature, and other properties). A parcel is used to statistically represent the discrete phase of all of the drops in that parcel [10].

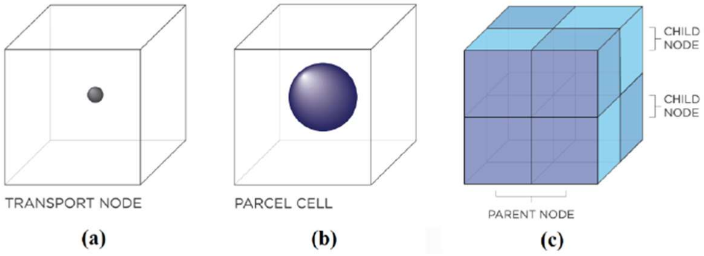

Fig. 6

Automatic grid generation involves moving the surface to the proper location (if the geometry includes moving components), trimming the boundary cells, refining any embedding areas, and then removing the refinement from the embedding. For stationary geometries, CONVERGE performs this process once at the start of the simulation and again whenever the geometry is refined or coarsened. For moving geometries, the grid generation process at each time-step is performed.

CONVERGE includes several tools for controlling the grid size before and during a simulation. Grid scaling coarsens or refines the base grid size. Fixed embedding refines the grid at specified locations and times. Adaptive Mesh Refinement (AMR) automatically changes the grid based on fluctuating and moving conditions.

CONVERGE employs an octree data structure for grid refinement. During a grid refinement process (fixed embedding or Adaptive Mesh Refinement), a parent transport node is subdivided into eight (or multiples of eight) child nodes (Fig.6c).

3.3 Grid scaling and Fixed embedding

Grid scaling refers to changing the base grid size at specified times during a simulation. Grid scaling can greatly reduce runtimes by coarsening the grid during non-critical simulation times and can help capture critical flow phenomena by refining the grid at other times [7].

The base grid size dx_base is changed according to:

$$dx\_scaled = \frac{dx\_base}{2^{grid\_scale}}$$

Therefore, a negative $grid\_scale$ will coarse the grid, a positive one will refine it while $grid\_scale = 0$ will leave the grid unchanged.

Fixed embedding is the same, but the base grid size can be refined in specified regions of the domain where a finer resolution is critical to the accuracy of the results. The $embed\_scale$, however must be a positive integer, therefore the mesh can only be refined.

$$dx\_embed = \frac{dx\_base}{2^{embed\_scale}}$$

A specific time period for each fixed embedding can be specified, which can further reduce the computational time by refining the grid only for a portion of the simulation. Also, there are several specific types of fixed embedding:

1) Boundary embedding: provides finer grid near boundaries. For example, surfaces defining a combustion chamber (cylinder head, piston crown, liners) can be embedded to enable more accurate heat transfer simulation (Fig.7), or when simulating flow around a valve, extra resolution near the valve surface is useful to more accurately model the flow in this section of the domain.
2) Sphere embedding: a spherical area is embedded.
3) Cylinder embedding: a cylindrical or truncated conical area is embedded.
4) Nozzle and injector embedding: a conical area is embedded around a nozzle (nozzle embedding), or a conical area is embedded around all nozzles of an injector (injector embedding). This type of embedding is especially useful to accurate modeling of sprays. Example of the nozzle embedding is shown in Fig.7
5) Box embedding: an area confined in a "box" is embedded.
6) Region embedding: the entire region of a domain is embedded. For example, the region embedding can be used to refine the grid in the cylinder of an engine.

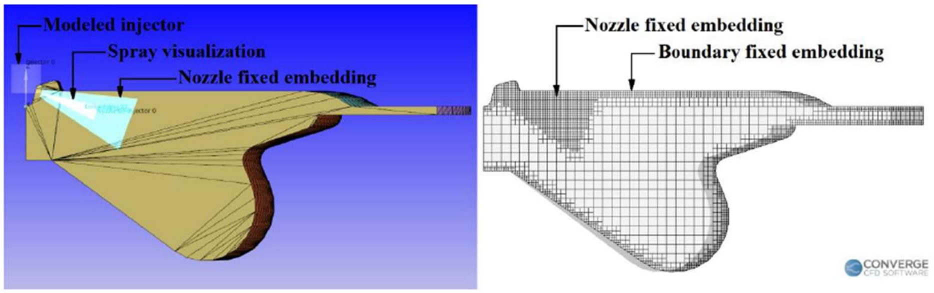

Fig. 7 – Fixed embedding example

3.4 Adaptive mesh refinement

Adaptive Mesh Refinement (AMR) automatically refines the grid based on fluctuating and moving conditions such as temperature or velocity. This option is useful for using a highly refined grid to accurately simulate complex phenomena such as flame propagation or high-velocity flow without unnecessarily slowing the simulation with a globally refined grid.

Ideally, a good AMR algorithm will add higher grid resolution (embedding) where the flow field is most under-resolved or where the sub-grid field is the largest (i.e., where the gradient of a specified field variable is the highest). The AMR method in CONVERGE estimates the magnitude of the sub-grid field to determine where embedding will be added [7]. Different fields, like velocity, temperature and number of parcels per cell, can be defined to activate the AMR. Moreover, the user can define different embedding scale, sub-grids and activation time for each AMR criteria.

In Fig.8 an example of AMR, using temperature, velocity and number of species as criteria, is reported

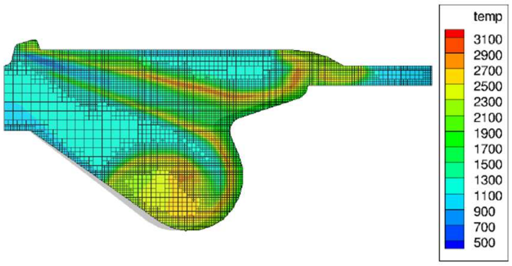

Fig. 8

3.5 Adaptive collision mesh

Collision calculations can be highly grid-sensitive when an under-resolved fluid-phase mesh is used. To address this issue, an adaptive collision mesh option has been implemented in CONVERGE.

In a simulation without collision mesh, parcels collide only with parcels in the same grid cell. This can lead to artifacts in the spray, since parcels do not collide across cell walls. This can also slow down computational time because there can be many parcels in larger cells. Using a collision mesh can eliminate both these problems. Simulations with collision mesh can much more accurately represent the spray dispersion by eliminating grid effects. However, the caution should be used when decreasing the collision mesh cell size: parcels can pass right through a collision mesh cell without having the chance to collide if the collision mesh to too refined.

The collision mesh is a uniform grid, used only for parcel collision, that rotates about a random axis at every time-step. The embed level of the collision mesh (set by the coll_scale parameter) is the number of levels below the base mesh size. The new grid size can be calculated with the equation for the fixed embedding.

This mesh is completely independent of the fluid-phase mesh and is used only for collision calculations. The algorithm for creating the collision mesh is based on randomly selecting a coordinate system and creating a collision mesh at each time-step. Once the mesh is created, the parcels are placed in the appropriate collision mesh cell and the collision calculation proceeds as usual [7].

3.6 Combustion modeling

CONVERGE implements the SAGE detailed chemical kinetics solver, presented in [11], which models detailed chemical kinetics via a set of CHEMKIN-formatted input files.

A chemical reaction mechanism is a set of the elementary intermediate reactions that compose an overall chemical reaction. Therefore oxidation of different fuels can be modeled implementing mechanism. SAGE calculates the reaction rates for each elementary reaction while the CFD solver solves the transport equations. Given an accurate mechanism, SAGE (in addition to AMR) can be used for modeling many combustion regimes (ignition, premixed, mixing controlled) [7].

As described by Turns [12], a multi-step chemical reaction mechanism can be written in the form:

$$\sum_{m=1}^{M} \nu'_{m,r}\chi_m \leftrightarrow \sum_{m=1}^{M} \nu''_{m,r}\chi_m \qquad for\, r = 1, 2, \dots, R$$

Where $\nu'_{m,r}$ and $\nu''_{m,r}$ are the stoichiometric coefficients for reactants and products, respectively, for species m and reaction r. R is the total number of reactions and χ_m is the chemical symbol of m.

The net production rate of the specie m can be expressed as:

$$\dot{\omega}_m = \sum_{r=1}^{R} \nu_{m,r} q_r \qquad for\, m = 1, 2, \dots, M$$

Where M is the number of total chemical species, and $\nu_{m,r} = \nu''_{m,r} - \nu'_{m,r}$.

The rate of progress for the r-th reaction q_r is defined as:

$$q_r = k_{fr} \prod_{m=1}^{M} [X_m]^{\nu'_{m,r}} - k_{rr} \prod_{m=1}^{M} [X_m]^{\nu''_{m,r}}$$

Where $[X_m]$ is the molar concentration of the species m and k_{fr} and k_{rr} are the forward and reverse rate coefficients for reaction r.

The forward coefficients, in SAGE modelling, is defined with the Arrhenius form:

$$k_{fr} = A_r T^{b_r} e^{\left(\frac{E_t}{\mathcal{R}T}\right)}$$

The reverse coefficient can be calculated from the equilibrium coefficient K_{cr}:

$$k_{rr} = \frac{k_{fr}}{K_{cr}}$$

Where the equilibrium coefficient is defined as function of the thermodynamic properties:

$$K_{cr} = K_{pr} \left(\frac{p_{atm}}{RT}\right)^{\sum_{m=1}^{M} \nu_{m,r}}$$

The equilibrium constant, K_{pr} is obtained as well as function of thermodynamic properties:

$$K_{pr} = \exp\left(\frac{\Delta S_r^0}{R} - \frac{\Delta H_r^0}{RT}\right)$$

Where Δ refers to the change that occurs in passing completely from reactant to products in the r-th reaction and S and H denote, respectively, entropy and enthalpy. Specifically:

$$\frac{\Delta S_r^0}{R} = \sum_{m=1}^{M} \nu_{m,r} \frac{S_m^0}{R}$$

and

$$\frac{\Delta H_r^0}{RT} = \sum_{m=1}^{M} \nu_{m,r} \frac{H_m^0}{RT}$$

It should be noticed that the reverse coefficient can be as well defined with the Arrhenius form in an analogous way of the forward coefficients. Moreover, the thermodynamic properties in the presented equations are all listed, in CHEMKIN format, in a *therm.dat* file that is part of the chemical reaction mechanism.

With the above information, the governing equations for mass and energy conservation can be solved for a given computational cell. The governing equation for mass and energy are, respectively:

$$\frac{d[X_m]}{dt} = \dot{\omega}_m$$

And

$$\frac{dT}{dt} = \frac{V\frac{dp}{dt} - \sum_m(\bar{h}_m \dot{\omega}_m)}{\sum_m([X_m]\bar{c}_{p,m})}$$

Where V is volume, T is temperature, p is pressure, $\bar{h}_m$ is the molar specific enthalpy and $\bar{c}_{p,m}$ the molar specific constant-pressure heat.

Last equation expresses the temperature variation for constant-volume combustion. At each computational time-step the SAGE model solves the above equations and the species are consequently updated. The temperature calculated from last equation is used to update the calculations in the SAGE model but is not used to update the CONVERGE cell temperature: this is, in fact, updated after the chemistry calculation has converged using the computed species concentrations. In order to speed up the chemistry calculations, kinetics is not solved in cells that fall below a minimum temperature (T_{cut}) or a minimum mole fraction (HC_{min}).

3.7 Emission modeling

CONVERGE offers different models to simulate soot and NO_x formations. In this work the nitric oxides production has been calculated via the SAGE chemistry solver, while for soot an empirical model, the Hiroyasu-NSC, and a detailed model, the particulate mimic, have been used.

Soot formation is quite a complex process, comprising several steps:

1) Inception: is the formation of the smallest solid soot particles from the gas-phase hydrocarbon molecules such as the polycyclic aromatic ones. This step is the link between the gas-phase chemistry and the soot particles dynamic
2) Surface growth: due to heterogeneous reactions on surfaces, both soot mass growth and soot particles loss is possible.

3) Coagulation: it's the physical process of collisions between small soot particles leading to the formation of larger soot particles.
4) Condensation: is when the gas phase species (such as PAHs) coagulate together and form large soot particles.

Fig.9 reports a schematic representation of the soot formation.

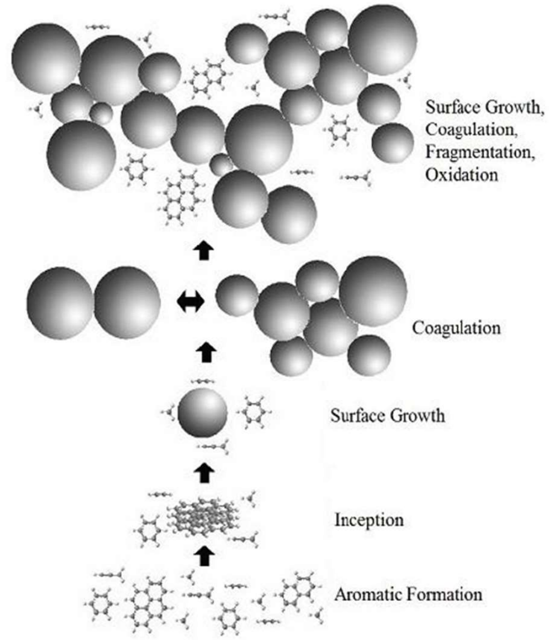

Fig. 9 – Soot formation process

The Hiroyasu-NSC empirical model determines the soot mass (M_s) production from a single-step competition between the soot mass formation rate ($\dot{M}_{sf}$) and the soot mass oxidation rate ($\dot{M}_{so}$):

$$\frac{dM_s}{dt} = \dot{M}_{sf} - \dot{M}_{so}$$

Where the formation rate is expressed as

$$\dot{M}_{sf} = SF \cdot M_{form}$$

M_{form} is the mass of soot formation species, while SF is a reaction coefficient expressed in the Arrhenius form. Two options are available for the soot formation species: first one is to consider all hydrocarbon species as soot formation species and is available for all combustion models. The second one uses C_2H_2 as soot formation species and requires a detailed chemical combustion models like the SAGE model.

The particulate mimic (PM) model is a detailed soot model and applies a comprehensive mathematical description for the soot particle size distribution (PSDF) and solve the complex soot formation and oxidation with detailed chemistry. Detailed soot models feature good capability over wide ranges of operating conditions. The properties of a soot ensemble can be described by the particle size distribution function (PSDF). The PSDF of soot can be obtained by solving equations for the number density of all size classes, based on the condition that the different physical and chemical processes changing the PSDF are known. This results in an infinite set of partial differential equations. Therefore, the size of the problem must be reduced using certain mathematical methods.

The method of moments is based on the fact that solving an infinite set of equations for the statistical moments of the PSDF is equivalent to the direct simulations of the PSDF. This method can be shown to have sufficient accuracy using only a few moments for global observables, such as mean number density and soot mass. Usually a set of equations for the first two to six moments is applied. The accuracy of the approach increases with the number of moments used. The main advantages of the method of moments is its computational efficiency and that the major features of the PSDF, such as mean number density and soot volume fraction, can be extracted from the moments. The Particulate Mimic (PM) model in CONVERGE is based on the method of moments introduced above [7]. The basic physical and chemical processes assumed to be important for the formation of soot are: particle inception, coagulation, condensation, and heterogeneous surface reactions, i.e., surface growth and oxidation by OH and O2. The dynamics of the soot particle characteristics can be described by a set of equations for the moments of the soot particle size distribution function:

$$\frac{dM_r}{dt} = \dot{M}_{r,pi} + \dot{M}_{r,con} + \dot{M}_{r,coag} + \dot{M}_{r,sr}$$

Where $\dot{M}_{r,pi}$, $\dot{M}_{r,con}$, $\dot{M}_{r,coag}$, $\dot{M}_{r,sr}$ are the rates of particle inception, condensation, coagulation and surface reactions for the r-th moment of the PSDF, respectively.

The moments are defined as:

$$M_r = \sum_{i=1}^{\infty} i^r N_i$$

Of course, the results from the Particulate-Mimic models are consistent with those deriving from the Hiroyasu-NSC model.

3.8 Spray modeling

The simulation of the spray injection is done introducing drop parcels into the domain at the injector location at a user-defined rate. Parcels represent a group of drops with the same parameters (i.e., same radius, velocity, temperature, etc.) and statistically represents the entire spray field. Adopting this concept, CONVERGE significantly reduces the computational time.

Spray droplets are subject to different processes between the injection time and their vaporization: breakup, collision and coalescence, turbulent dispersion. Also the nozzle characterization affects the droplets.

3.8.1 Nozzle discharge coefficient

Contraction effects of nozzles are accounted in each injector, depending on the user inputs for discharge coefficient, nozzle diameter, liquid density, injection rate-shape, injected mass and injection duration. The contraction coefficient, C_a, of a nozzle is given as:

$$C_a = \frac{C_d}{C_v}$$

Where C_d and C_v are the discharge and velocity coefficients respectively. These are dynamically calculated from injection pressure.

The area contraction coefficient accounts for cavitation or hydraulic flip effects which can lead to a reduced flow area at the nozzle exit [11]. The effective diameter of the nozzle, d_{eff}, is calculated from the geometrical nozzle diameter, d_{geom}, as:

$$d_{eff} = \sqrt{C_a} d_{geom}$$

Since the first injected drop is equal to the nozzle diameter, the reduce d_{eff} means that also the initial parcel size is reduced and therefore the drop velocity magnitude increases proportionally.

Injection pressure is then expressed as:

$$P_{inj} = \frac{1}{2} \rho_l \left(\frac{V}{C_d} \right)^2$$

Where ρ_l is the liquid density and V is the liquid velocity based on the geometric hole diameter. As the premixed combustion phase is directly affected by the injection pressure, it's evident that a correct characterization of the nozzle discharge coefficient is a fundamental step of the numerical simulation.

3.8.2 Injection size distribution

Four injection size distributions are available in CONVERGE: blob, chi squared, Rosin-Rammler, and constant injected radius. Blob model is based on the size of a nozzle, while other three methods depend on the Sauter Mean Diameter (SMD), which has to be specified by the user.

Blob is described as discrete parcel of drops, which has the same diameter as nozzle exit diameter (or effective nozzle diameter). This blob injection method of prescribing atomization differs from those other three, which assume that the liquid is already finely atomized at the nozzle exit with an initial distribution of drop sizes at the nozzle assumed with the SMD. The assumption of immediate atomization at the nozzle exit does not account for the presence of a core within a high-pressure spray [13]. It is known that there is an "intact core" of largely unbroken liquid which can extend for hundreds of nozzle diameters. A core region is predicted with the blob injection method. This is because the injected blobs breakup due to interaction with the surrounding gas as they penetrate, yielding a region of relatively large drops near the nozzle [13]. Schematic showing the conceptual liquid flow structure at the nozzle exit for diesel-type sprays is given in Fig.10.

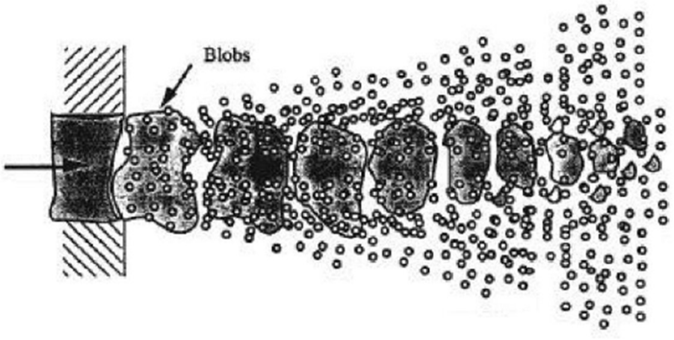

Fig. 10

3.8.3 Drop drag

Accurate determination of drop drag coefficients is critical for accurate spray modeling. CONVERGE includes two models for drop drag (in addition to the option of no drag). The first model calculates the drag coefficient with the assumption that the drops are perfect spheres. The second model, called the dynamic drag model, determines the droplet drag coefficient dynamically, accounting for variations in the drop shape through a drop distortion parameter y. Values of the drop distortion parameter are determined from the Taylor Analogy Breakup (TAB) model, detail description of which is given in [7].

As an initially spherical droplet moves through a gas, its shape will distort significantly when the Weber number (a dimensionless parameter defined as the ratio of aerodynamic forces to surface tension forces) is large. In the extreme case, the drop shape will approach that of a disk. The drag on a disk is significantly higher than that of a sphere. Since the drop drag coefficient is highly dependent on the drop shape, a drag model that assumes the drop is spherical can under-predict drag. The dynamic drag model accounts for the effects of drop distortion by linearly varying the drag between that of a sphere, and a value corresponding to a disk [7].

The drag coefficient is given by:

$$C_D = C_{D,sphe} \quad (1 + 2.632y)$$

Where y is the drop distortion parameter determined from the TAB model.

3.8.4 Spray breakup

CONVERGE includes several spray breakup mechanisms, including models based on the Kelvin-Helmholtz (KH) and Rayleigh-Taylor (RT) instability mechanisms, the Taylor Analogy Breakup (TAB) drop breakup model, and the LISA (Linearized Instability Sheet Atomization) sheet breakup model.

The TAB model is best for low Weber-number sprays. It does not provide reasonable predictions for the characteristics of high-pressure sprays and simulated engine performance and emissions. TAB based models has been found to predict a quite small premixed combustion phase and a large diffusive combustion phase due to their over prediction of droplet breakup [14].

The LISA model is used to model liquid sheet breakup. The model includes two parts – a general liquid sheet breakup mechanism and a liquid injection methodology specifically for pressure-swirl atomizers. The pressure-swirl atomizers are widely used for liquid-fuel combustion in gas turbines, oil furnaces, and direct-injection spark-ignition automobile engines.

Finally, spray breakup models based on both Kelvin-Helmholtz (KH) and Rayleigh-Taylor (RT) instability are usually used together in a combined model, KH-RT. A version of it, called the modified KH-RT breakup model, has been found to be especially accurate in engine simulations [14]. This model is also available in CONVERGE and has been used in this thesis.

The Kelvin-Helmholtz instability is based on a liquid jet stability analysis that is described in detail in [15]. The analysis considers the stability of a cylindrical, viscous, liquid jet of radius r_0 issuing from a circular orifice at a velocity U into a stagnant, incompressible, inviscid gas of density ρ_g. The liquid has a density ρ_l and viscosity μ_l and a cylindrical polar coordinate system is used which moves with the jet [7].

In the KH model, the initial parcel diameters are set equal to the nozzle hole effective diameter d_0 (or d_{eff}) and the atomization process of the relatively large injected blobs is modeled using the stability analysis for liquid jets. The breakup of the parcels and resulting drops is calculated by assuming that the breakup drop radius r_c is proportional to the wavelength of the fastest growing unstable surface wave Λ_{KH}:

$$r_c = B_0 \Lambda_{KH}$$

Where B_0 is a model constant usually set as 0.61: if necessary it can be adjusted.

The drop radius variation rate is calculated as:

$$\frac{dr_p}{dt} = -\frac{(r_p - r_c)}{\tau_{KH}} \quad , \qquad r_c \leq r_p$$

Where τ_{KH} is the breakup time, defined as:

$$\tau_{KH} = \frac{3.762 B_1 r_p}{\Lambda_{KH} \Omega_{KH}}$$

Where Ω_{KH} is the maximum growth rate of the instability waves and B_1 is the breakup time constant: this has been found to be related to the initial disturbance of the liquid jet and to vary from one injector to another[16]. The KH model can be set with the creation of new child parcels. After the break-up of a droplet, pieces of it fragment away: when these pieces accumulate enough mass (defined by the flag *newparcel_cutoff*) CONVERGE consider them as a new parcel with a drop size of radius r_c.

The fragmented mass is defined as:

$$\sum_n sN^n \frac{4}{3} \pi \rho_l [(r_p^n)^3 - (r_p^{n+1})^3]$$

Where *s* is the shed factor and represent the fraction of the parent parcel that contributes to the mass of the child parcel: in simple terms, a high shed factor means that more child parcels will be created. Also, as investigated by M.A. Patterson and R.D. Reitz in "*Modeling the Effects of Fuel Spray Characteristics on Diesel Engine Combustion and Emission*", an overestimation of the shed mass, due to the formation of many child parcels, will result in a rapid reduction of the Sauter Mean Diameter (SMD) and can lead to errors on mass conservation.

In the figure below, the numerical results of the SMD with two different shed factors are reported.

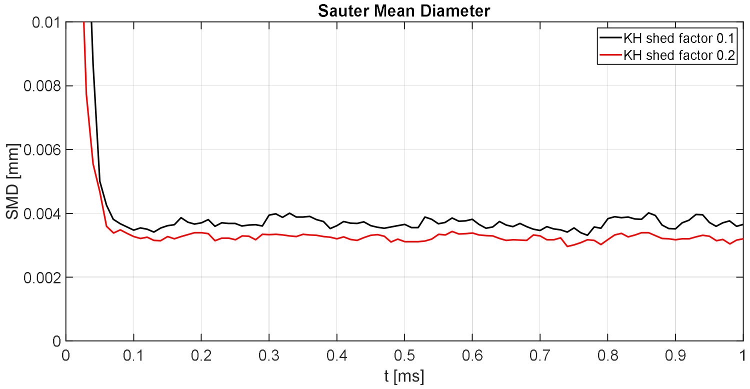

Fig. 11 - Numerical results from non-reacting simulations of a nC12 spray, with a mesh size of 0.125 mm

The Rayleigh-Taylor mechanism is based on the unstable waves that occur due to rapid drops deceleration from magnitude of the drag force, $|F_{D,i}|$. These are calculated as:

$$|F_{D,i}| = m_d |a_i| = m_d \frac{3}{8} C_D \frac{\rho_g |U_i|^2}{\rho_l r_0}$$

Where m_d is the drop mass, $|U_i|$ drop velocity, $|a_i|$ drop acceleration, C_D the drag coefficient and ρ_g and ρ_l the gas and liquid density, respectively.

Typical implementations of the RT breakup model ignore both gas and liquid viscosity. CONVERGE spray models extend the standard RT model to include viscosity, which can have a large effect for the high decelerations typical of spray droplets. Description of calculation steps for the fastest growing wavelength, Λ_{RT}, and the corresponding growth rate, Ω_{RT}, are given in [7]. If the scaled wavelength given by $C_{RT}\Lambda_{KH}$is calculated to be smaller than the droplet diameter, RT waves are assumed to be growing on the surface of the drop. When the RT waves have been growing for a sufficient time (i.e., for the RT liquid breakup time τ_{RT}=C_I/Ω_{RT}, where C_I is a constant), the drop is broken up according to the RT mechanism. Note that the RT model size constant CRT can be increased or decreased to change the size of the predicted RT breakup. Similarly, the RT model breakup time constant CI can be increased to delay RT breakup, or decreased to promote faster RT breakup.

CONVERGE offers the possibility to model with both the mechanisms: as reported in Fig.12 in the first part of the spray, defined as break-up length, only the KH instability mechanism is active. After that, both the KH and the RT mechanisms affects the break-up.

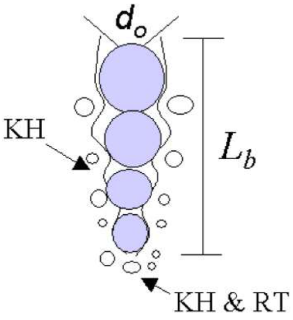

Fig. 12

After the characteristic breakup distance L_b, when both of the mechanisms are activated, COVNERGE first checks if the RT mechanism can result in the droplet breakup. If not, the KH mechanism is responsible for breakup.

The breakup length, L_b is defined as:

$$L_b = C_{bl} \cdot \sqrt{\frac{\rho_l}{\rho_g}} \cdot d_0$$

Where C_{bl} is the breakup length constant: this can be tuned as described by Senecal(2000) [ref]

3.8.5 Drop collision

If the drop collision is activated, CONVERGE offers two collision models (O'Rourke and NTC) and two model for collision outcomes (O'Rourke and Post).

The No Time Counter (NTC) method is described in [17]. This is based on techniques used in gas dynamics for Direct Simulation Monte Carlo (DSMC) calculations.

The NTC method involves stochastic (randomly determined) sub-sampling of the parcels within each cell. This potentially results in much faster collision calculations. Unlike O'Rourke's method, which assumes that multiple collisions can occur between parcels and that this process is governed by a Poisson distribution. However, the Poisson distribution is not correct unless collision has no consequences for the parcels. Since collisions change parcels' velocities, size, and number, the method of repeated sampling used in the NTC model generates more accurate answers [17]. Moreover, the NTC model presents a linear relation between the computational cost and the parcel number, while O'Rourke computational cost increases with the square of the parcel number. Therefore the NTC model has been shown to be faster and more accurate than O'Rourke's model under certain conditions [7].

The NTC method is derived, without assumptions, from the basic probability model for stochastic collision. The basic probability model requires that the cell size is sufficiently small in order to neglect spatial variation in spray. These assumptions are a subset of those required for deriving the O'Rourke collision model.

The NTC method first sorts the parcels into groups that reside in the same cell. This requires only 2N operations, where N is the number of droplets in a cell. Next, the NTC method picks a random subsample from all of the possible pairs in a cell. The probabilities for the sub-sample pairs are multiplied by the reciprocal of this fraction, increasing the probability of collision. Sampling is done with replacement so that multiple collisions for a pair can be correctly calculated. The resulting method incurs a cost that is linearly proportional to the number of parcels, as opposed to the N-squared cost of many existing methods. A detailed derivation can be found in [17].

As said, the collision outcomes can be modeled with the O'Rourke or the Post models. The O'Rourke Collision scheme can result in grazing collisions or in coalescence. In addition to this, Post and Abraham [18] included both stretching separation and reflexive separation in their model based on experimental results of hydrocarbon drops. This model is called Post collision outcomes.

In this model, first it is checked if the collision of two drops would result in a bounce. If yes, the post bounce velocities are calculated for both drops. In other case, either permanent coalescence, stretching separation, or reflexive separation take place. Detailed description can be found in [7].

3.8.6 Drop turbulent dispersion

CONVERGE models the effects of the turbulent flow on spray drops by adding a fluctuating velocity u_i' to the gas velocity u_i.

u_i' is described using RANS or LES turbulence model (when used). RANS turbulence models in CONVERGE includes source terms to account for the depletion of turbulent kinetic energy due to work done by turbulent eddies to disperse the liquid spray droplets. The source terms include the fluctuating component of the fluid-phase velocity u_i'. Then, ui' can be determined by two models [7]:

1) O’Rourke model: it is assumed that each component of u_i' follows a Gaussian distribution.
2) TKE (turbulent kinetic energy) preserving model: model chooses each component of u_i' such that $|u_i'| = \sqrt{2k}$ (where k is the cell turbulent kinetic energy).

More detailed description of both models can be found in [7]. In this work, O’Rourke model is used for the drop turbulent dispersion modeling.

3.8.7 Drop/wall interactions

CONVERGE offers three options for modeling drop/wall interaction [7]:

1) Rebound/Slide Model: model includes two impingement regimes, rebound and slide, based on the Weber number, Wei, of the incoming drop at impact. If Wei is less than 80 (rebound regime), the drop rebounds elastically with a normal velocity. If Wei is greater than 80, the jet model is used to update the drop velocity. In this model, the sheet thickness produced from an impinging liquid jet is calculated.
2) Wall Film Model: it is a particle-based wall film for modeling the interaction of liquid drops with solid surfaces. The model uses a hybrid approach to film modeling: some calculations assume individual particle-based quantities, while other calculations assume film-based quantities. For example, the thickness of the film on wall face α, which is used throughout the film model, is given by:

$$h_\alpha = \frac{\sum_p V_p}{|A_{\alpha,i}|}$$

   Where $V_p$is the p parcel volume, $A_{\alpha,i}$ is the area projection vector of face α

3) Drop Vanish Model: with this model activated the spray droplets vanish as they impinge on the wall boundary. The mass of drops disappears from the simulation in such an instance. This is not the same as drop vaporization.

In this work, the Wall Film model is adopted. The film momentum equation is used to model liquid film transport. However, it is used to update velocities of particles that impinged on a solid surface in a previous time-step. If a particle has just impinged on a wall in the current time-step, CONVERGE calculates its velocity with the jet model as in the Rebound/Slide model (rebound Weber number can be set by user). The Wall Film model also takes into account drop/film splashing. Three models are available: O’Rourke, Kuhnke, and Bai-Gosman. In this work O’Rourke model is chosen. Detailed description for all three models can be found in [7].

The Wall Film model includes two other effects: film separation and film striping (if enabled). Film separation can occur if wall film particles flow over a sharp corner. The separation criterion is used to determine if film separation takes place: if yes, the film parcels are converted to spray parcels with a diameter equal to the film thickness. Film stripping takes place due to the growth of waves on the surfaces caused by the aerodynamic forces acting on the film. Once the waves reach a critical amplitude, fragments of the liquid are broken off which contract to form cylindrical ligaments that are believed to move normal to the ligament axis. As a result, capillary forces cause the unstable ligaments to break into drops.

3.8.8 Vaporization

CONVERGE contains vaporization models to determine how the radius of a drop changes over time. The Frossling correlation and the Chiang correlation are available. Also, droplet boiling model can be enabled. Finally, CONVERGE contains two methods for computing thermal transfer to a drop: Uniform Temperature model and Discretized Temperature model [7]. In this work, Frossling correlation with droplet boiling model is used. Thermal transfer to a drop is calculated using the Discretized Temperature model.

The Frossling correlation express the radius variation as:

$$\frac{dr_0}{dt} = -\frac{\alpha_{spray}\rho_g D}{2\rho_l r_0} B_d Sh_d$$

Where α_{spray} is the scaling factor for the mass transfer coefficient (user-defined), D is the mass diffusivity of the liquid vapor in air. ρ_l and ρ_g are the liquid and gas density, respectively. Sh_d is the Sherwood number.

The coefficient B_d is defined as:

$$B_d = \frac{\gamma_1' - \gamma_1}{1 - \gamma_1'}$$

Where γ_1' is the vapor mass fraction at the drop surface and γ_1 is the vapor mass fraction.

As the droplet reaches its boiling temperature, CONVERGE calculates the radius variation as:

$$\frac{dr_0}{dt} = \frac{k_{air}}{\rho_d c_{p,air} r_0}\left(1 + 0.23\sqrt{Re_d}\right)\ln\left[1 + \frac{c_{p,air}(T_{air} - T_d)}{h_{fg}}\right]$$

Where k_{air} is the air thermal conductivity, $c_{p,air}$ the specific heat capacity, Re_d is the droplet Reynolds number and h_{fg} is the heat of vaporization.

A full and complete description of this model is available in [7].

4 SURROGATE FUEL

4.1 Introduction

As the automotive industry is pushed to a continuous innovation, computational fluid dynamics (CFD) calculations for internal combustion engines (ICEs) have become a fundamental resource for power-train designers to optimize the engine in terms of efficiency, performance and pollutant emissions. In addition to engine optimization, fuels as well have been improved and new ones, like hydrotreated vegetable oil (HVO), have been introduced. In numerical simulations, the combustion process is modelled thanks to kinetic oxidation mechanisms in which the numerous intermediate reactions that occur during the combustion of fuel are listed and coupled with thermodynamics and transport properties such activation energy or standard enthalpy of combustion. However, real fuels comprise of hundreds if not thousands of chemical compounds, each affecting both physical and chemical properties and, therefore, the vaporization and combustion behaviour of the said fuels. Due to the large scale of species present in fuel, it is quite a humongous task to model all of them numerically and is beyond the reach of engine level CFD applications. Moreover biofuels can be produced starting from different feedstock, resulting in different compositions: experimental development of a chemical kinetic model results to be excessively time consuming and, therefore, can’t keep up with the pace of fuel innovation.

Surrogate fuels are a mixture of relatively few, well characterized chemical compounds, developed to successfully mimic the targeted properties and combustion behaviour of the real fuel. The associated chemical kinetic mechanisms allow to model the oxidation process of the fuel within CFD simulations. Recent development of kinetic mechanisms for n/iso-alkanes with carbon chains up to C16 and other, more complex, hydrocarbons, in Lawrence Livermore National Laboratories (LLNL) has given the opportunity to develop and study new more accurate surrogates for diesel-like fuels with respect to previous ones.

4.2 Surrogate selection approach

Research on surrogate formulation has been an active field of study over the last decades and can be divided into two main categories. One focuses on matching physical, chemical and combustion properties of the real fuel: therefore properties such as density, volatility and cetane number are target of the analysis. The other category of surrogate formulation focus on the direct emulation of the active functional groups like methyl, propyl and ester groups. The approach developed in this thesis belongs to the first group. However, it should be mentioned that, even though great discrepancies between the two sets of approaches, the goal is to optimize the CFD simulations, reducing the inconsistencies between surrogate and target fuel, and the computational power required.

Since this thesis focuses on diesel application and the approach is based on matching the physical and combustion related properties of the target fuel, a brief description of diesel combustion is reported, in order to choose the right properties to match.

Diesel combustion is composed of several phases:

- Ignition delay period:
- Premixed combustion
- Mixing controlled combustion
- Late combustion phase

Fuel injected into the chamber goes through a series of physical and chemical processes during ignition delay period. First, the jet breaks down into smaller droplets: fuel properties like density, surface tension and viscosity effects this phase. Next, there's the fuel droplets evaporation which is strongly dependent on the fuel volatility and charge temperature. Then follows the mixing of vaporized fuel with air, creating a combustible mixture which is strongly affected by turbulent mixing, species diffusivities and combustion chamber geometry. To this follows the chemical process where fuel is decomposed into smaller hydrocarbons and active radicals that initiates the spontaneous ignition of the mixture leading to premixed phase. This phase is driven by the fuel properties like cetane number for diesel applications. Local air/fuel ratio and adiabatic flame temperature are influenced by the C/H ratio.

Therefore, the following properties has been selected as target to create a surrogate fuel that mimic properly the real fuel.

- Cetane Number (CN)
- Distillation curve
- C/H mass ratio (C/H)
- Density (ρ)
- Viscosity (μ)
- Lower Heat of Combustion (LHC)

Below, in Fig.1, the flow chart reports the validation process of the surrogate formulation approach proposed in this thesis.

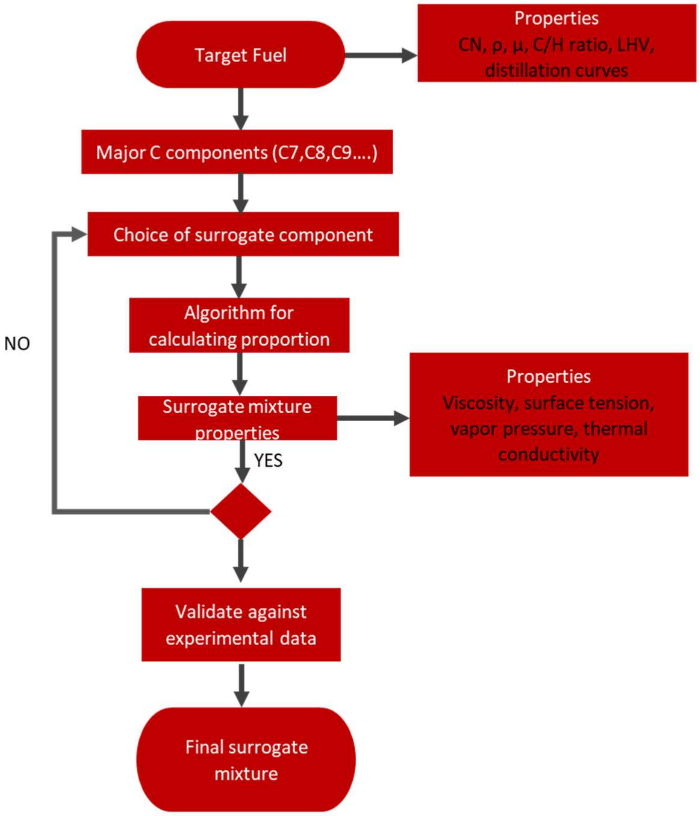

Fig. 13

Once the target fuel and properties are defined, its major components, based on carbon chains, are identified and so a list of suitable chemical components is generated. Than an algorithm for calculating proportions is used and a surrogate mixture is defined. The CONVERGE CFD software requires other properties, such as vapor pressure and surface tension, to run a numerical simulation: these properties are used as first validation on the proposed surrogate mixture, checking the discrepancies between target and surrogate fuel.

The resulting mixture is then implemented in two simulations with the objective of reproducing experimental data obtained from the Engine Combustion Network (ECN) platform. Two conditions are simulated: the first one is a non-reacting case, therefore the ambient O_2 concentration is 0%. The second one is a reacting case with an oxygen concentration of 15%. Experimental setup will described more in detail in the spray calibration section.

4.3 Surrogate formulation algorithm

The algorithm proposed is based on a methodology first proposed by Li et al. [19] and it uses the Euclidean Distance to evaluate the matching of target fuel properties. In a N-dimensional space, where N is the number of constraints on surrogate formulation (so, the target properties) the target and the surrogate fuel can be represented as two vectors and the objective of the algorithm is to find the mixture that can minimize the euclidean distance between them. The vector representing the surrogate fuel, is defined with an estimation method that calculates the properties according to the molar, volume and mass fractions of the components.

In Fig. 2 a graphic representation of this method is presented (considering a ternary mixture), while in Tab. 1 the estimation methods to calculate the properties are reported.

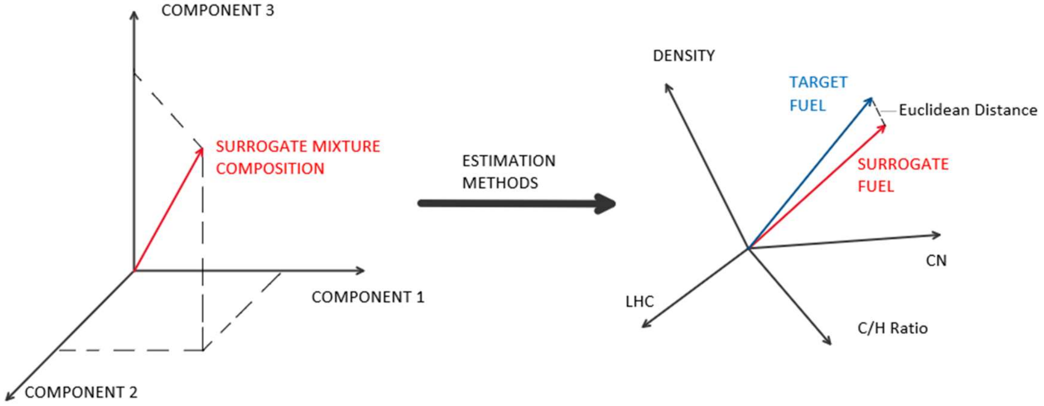

Fig. 14

Parameter	Estimation
Density	$\rho_{mix} = \sum \nu_i \cdot \rho_i$
Cetane Number	$CN_{mix} = \sum \nu_i \cdot CN_i$
Lower Heat of Combustion	$LHC_{mix} = \sum \gamma_i \cdot LHC_i$
C/H mass ratio	$CH_{mix} = \sum \chi_i \cdot CH_i$

ν_i, γ_i, χ_i are respectively volume, mass and molar fraction of the i-component

Tab. 1

The algorithm is created through a simple MATLAB script that allows to create surrogate mixture compositions with variation in volume fraction of 1% per component and the consequent molar and mass fractions. For each composition generated, the target properties are calculated (using the estimation methods reported in Tab.1) and the Euclidean distance from target fuel vector is calculated with (Eq.1). The surrogate fuel mixture is therefore defined as the one with the minimum ED.

$$ED = \sqrt{\left(CN_{target} - CN_{mix}\right)^2 - \left(LHC_{target} - LHC_{mix}\right)^2 - \left(\rho_{target} - \rho_{mix}\right)^2 - \left(CH_{target} - CH_{mix}\right)^2} \quad \text{(Eq.1)}$$

Each property is calculated using temperature dependent equations found in Yaws' [20]: these are parametric equations, and for each chemical specie coefficients and a temperature range within which the equations are validated.

4.4 Traditional Diesel Surrogate

Traditionally, Diesel fuel has been represented using n-heptane, a linear alkane with a C7 carbon chain, as surrogate [21,22,23]. However, since the mean carbon content in diesel fuel ranges from 12 to 13, some have tried to use n-dodecane, also a linear alkane but with a C12 carbon chain, as surrogate [24].insert ref "prashant goel et al"]

As reported by W.J. Pitz et al [25] and C.J. Mueller et al [26] the composition of diesel fuel is essentially based on n-alkanes, iso-alkanes, cycloalkanes and aromatics as shown in Fig.3:

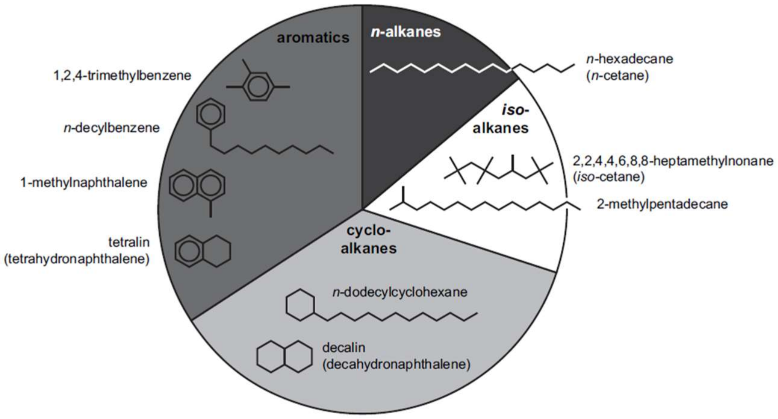

Fig. 15

It can be noticed that the composition of diesel fuel is highly variable, and using a multi-component mixture as surrogate fuel can result in an increased accuracy in numerical results from CFD simulations.

As reported by R. Lin and L.L. Tavlarides [27] at least twenty different diesel surrogates have already been proposed with up to 12 components (insert table?). However it should be noticed that adopting a surrogate mixture with that many components will require an enormous computational power and although the accuracy of the results will be higher, it's not objective of engine CFD applications such as the one in this thesis.

Since the experimental data that will be used to validate the surrogate derives from the ECN platform, the target diesel fuel properties also are taken from there. In Tab.2 [28] the tested fuels properties are reported, with traditional diesel labelled as D2.

FUELS	D2	JC	JW	JS	JP	SR*
	No. 2 Diesel	JP-8	World Average Jet A Blend	Fischer-Tropsch Fuel	Coal-Derived Fuel	Surrogate Fuel
T_{10} [°C]	211	170	180	167	192	
T_{90} [°C]	315	240	251	254	243	
T_{100} [°C]	350	266	274	276	270	216
Cetane Number	46	38	46	62	34	70
Lower heating value [MJ/kg]	42.975	43.228	43.2	44.138	42.801	43.33
Density at 15°C [kg/m^3]	843	812	806	755.9	870.2	778.9
C/H mass ratio	6.53	6.19	6.19	5.49	6.58	5.96
Stoichiometric Air/Fuel ratio	14.47	14.62	14.62	14.96	14.46	14.73
Aromatics volume %	27	11	19	0.4	1.9	23
Sulfur [ppm]	9	1	0	0	0	
Kin. Visc. (-20°C) [mm^2/s]	-	4.465	5.2	4.6	7.5	
Kin. Visc. (40°C) [mm^2/s]	2.35	~ 1.4				
Freeze Point [°C]	-	-57	-48	-51	-65	
Flash Point [°C]	73	47	51	45	61	

Tab. 2

Distillation curve has to be estimated using a linear interpolation from the three given point, representing the volume fraction evaporated at the relative temperature. However, an additional distillation curve is taken from Lapuerta et al [29]. It can be easily noticed how the evaporation of diesel requires higher temperatures with respect of other fuels reported.

As surrogate candidates, the following hydrocarbons have been selected:

n-hexane	(C_6H_{14} – nC6)
n-dodecane	($C_{12}H_{26}$ – nC12)
2-methylpentadecane	($C_{16}H_{34}$ – 2MP)
2,2,4-trimethylpentane	(C_8H_{18} – TMP/iso-octane)
2,2,4,4,6,8,8-heptamethylnonane	($C_{16}H_{34}$ – HMN)
Propylbenzene	(C_9H_{12} – nPB)
m-xylene	(C_8H_{10} – mX)
1-methylnaphthalene	($C_{11}H_{10}$ – 1MN)
Methylcyclohexane	(C_7H_{14} – MCH)
Propycyclohexane	(C_9H_{18} – PCH)
Decalin	($C_{10}H_{18}$ – DEC)

Three different mixtures, reported in Tab.3, have been investigated. The first one is based on the works of Pei et al.[30] and of Kook and Picket[28]: a mixture of m-xylene (23%) and n-dodecane (77%) is investigated because, compared to the neat dodecane, this binary blend, named SR23[28], contains an aromatic which represents an important chemical class in diesel composition. Starting from this 2-methylpentadecane (2MP) and methylclohexane (MCH) were added with the same purpose. Methylcyclohexane has been used as a surrogate component for diesel also in the work of Chang et al.[31]. Second mixture is the one investigated in the work of P. Dagaut[32]: this is to make a comparison between the volume fractions obtained with the presented approach and the ones Dagaut obtained in his work. Third mixture has been formulated in order to match not only the heterogeneous composition of Diesel, but also its high temperature distillation curve. This mixture presents, in fact, heavier compounds with respect to the others.

Mix.1	**MCH**	**mX**	**nC12**	**2MP**
vol. [%]	1 %	63 %	0 %	36 %
Mix.2	**nC6**	**TMP**	**PCH**	**nPB**
vol. [%]	1 %	0 %	40 %	59 %
Mix.3	**DEC**	**1MN**	**HMN**	**2MP**
vol. [%]	46 %	4 %	25 %	25 %

Tab. 3

Resulting properties for the three mixtures are reported and compared to target ones in Tab.4 below, while the resulting distillation points and the experimental distillation curves are represented in Fig.4.

	D2	**Mix.1**	**Mix.2**	**Mix.3**
CN	46	35.38	20.9	46.18
ρ	843	833.62	839.01	842.94
C/H (mass)	6.53	8.81	7.86	6.69
LHC	42.98	41.90	43.32	43.16

Tab. 4

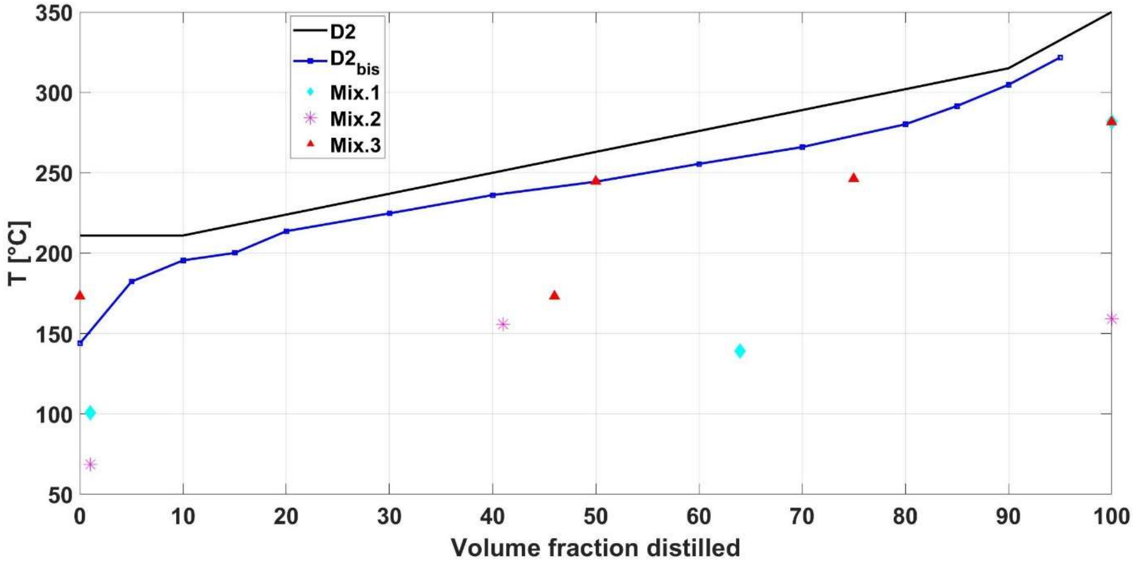

Fig. 16

In Fig.4, the D2 curve refers to data from [28], while the $D2_{bis}$ one refers to the work of La Puerta et al. [29].

It can be easily noticed how the third mixture (DEC-1MN-HMN-2MP) is the best one in terms of matching the properties. However, the resulting kinetic mechanism to model the oxidation process was too big even after the reduction, through a sensitivity analysis and isomer lumping, from the detailed one to the skeletal mechanism. Therefore the computational power required to perform numerical simulations resulted to be too high for the available resources. This issue has been solved using a different approach in numerical simulation consisting of considering as separated the liquid and the gaseous phases: this was possible thanks to the CONVERGE CFD feature.

The approach now has to be modified since two surrogates have to be defined for two different phases with different target properties. The gaseous phase has to match combustion related properties (cetane number, C/H ratio and lower heat of combustion). As presented in the work of D.L. Siebers [33] spray characteristics as liquid and vapor penetration are affected by the liquid density and volatility: therefore the surrogate for the liquid phase has to match those properties.

For the gas phase the following hydrocarbons have been considered:

n-decane	($C_{10}H_{22}$ – nC10)
n-dodecane	($C_{12}H_{26}$ – nC12)
2,2,4,4,6,8,8-heptamethylnonane	($C_{16}H_{34}$ – HMN)
Propylbenzene	(C_9H_{12} – nPB)
m-xylene	(C_8H_{10} – mX)

The combustion related properties of these components are reported in Tab.5

PROPERTY	UNIT	mX	nPB	nC10	nC12	HMN
CN	[-]	7	16	66.35	74.00	14.7
C/H ratio	[-]	9.608	9.008	5.459	5.543	5.651
LHC	[MJ/kg]	40.86	41.29	44.32	44.21	44.07

Tab. 5

The algorithm has been adjusted to use the three mentioned properties as target, and four different mixtures are investigated and presented in Tab.6, while in Tab.7 resulting properties are shown. It has to be mentioned that a kinetic mechanism for n-propylbenzene was already available at the Lawrence Livermore National Laboratories website, so although Mix.3 seems to have a better matching properties, Mix.4 has been selected as mixture.

MIXTURE	COMPONENT	VOLUME FRACTION
MIX.1	nC12	53%
	HMN	47%
MIX.2	nC10	61%
	HMN	39%
MIX.3	mX	18%
	nC12	55%
	HMN	27%
MIX.4	nPB	25%
	nC12	52%
	HMN	23%

Tab. 6

PROPERTY	**UNIT**	**MIX.1**	**MIX.2**	**MIX.3**	**MIX.4**
CN	[-]	46.13	46.2	45.93	45.86
C/H ratio	[-]	5.58	5.52	6.81	6.83
LHC	[MJ/kg]	44.14	44.22	43.5	42.98

Tab. 7

As mentioned above, the liquid phase surrogate has to mimic the spray characteristics, so the algorithm has been adjusted again: in this case target properties have been density, lower heat of combustion (adopted as control property) and volatility (distillation curve). As reported in Tab.8 it can be noticed that n-dodecane (with boiling temperature of 216.32 °C) has been added to the previous mixture.

MIXTURE	**COMPONENT**	**VOLUME FRACTION**
OLD SURROGATE MIX	DEC	46
	1MN	4%
	HMN	25%
	2MP	25%
LIQUID PHASE SURROGATE MIX	DEC	30%
	nC12	15%
	1MN	5%
	HMN	25%
	2MP	25%

Tab. 8

In Fig. 5 the new distillation points are reported: the new mixture is certainly better than the previous one in terms of volatility. However, as reported in Tab.9, there's an higher discrepancy in density which is no more matched -almost- perfectly.

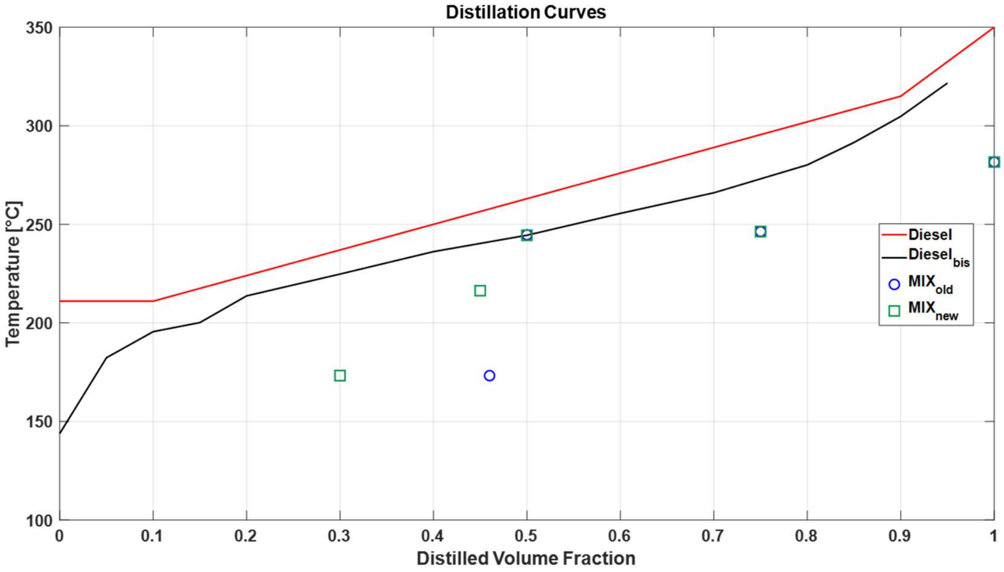

Fig. 17

	Diesel	Old surrogate mix	Liquid phase surrogate mix
DENSITY [kg/cm3]	843	842.94	821.93
LHC [MJ/kg]	42.98	43.16	43.34

Tab. 9

The higher approximation on density has been accepted in order to simplify calculations and proceed faster: moreover during the simulation phase it hasn't been a problem. However, future steps should consider this as a possible starting point to eventually improve the presented approach.

4.5 JS Fuel Surrogate

Since there's no experimental data regarding spray injection or combustion of the hydrotreated vegetable oil (HVO), a further validation of the model has been made using JS Fuel as target: as said in the introduction part, it's a Fischer-Tropsch (FT) fuel, from the developers of the production method. Fuels obtained using the FT process result to be characterized with minimal sulfur and aromatics content, high cetane number and a density lower than traditional diesel.

JS fuel properties are reported in Tab.2, which is reported again below to simplify the reading. JS is used as target fuel because of its composition (see Tab.11): as the HVO it's composed only of alkanes, both linear and branched. Moreover it presents similar characteristics in terms of spray and combustion related properties, as will be presented in the HVO surrogate paragraph. Therefore, the model developed to formulate and analyze the traditional diesel fuel (D2) surrogate will be further validated and tested.

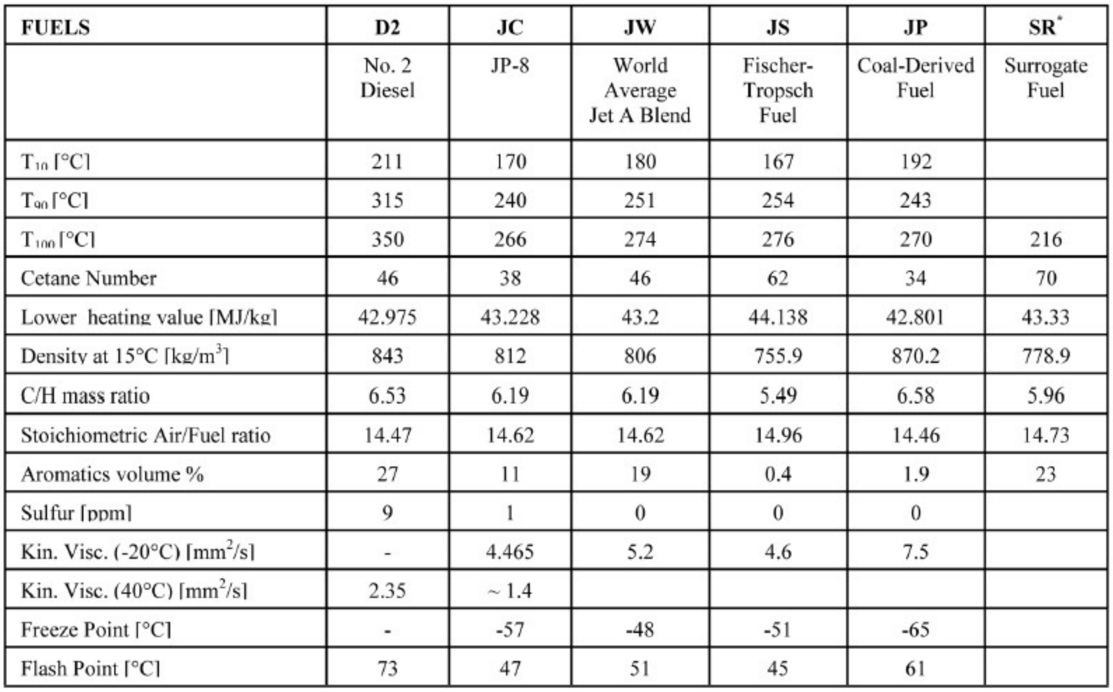

FUELS	D2	JC	JW	JS	JP	SR*
	No. 2 Diesel	JP-8	World Average Jet A Blend	Fischer-Tropsch Fuel	Coal-Derived Fuel	Surrogate Fuel
T_{10} [°C]	211	170	180	167	192	
T_{90} [°C]	315	240	251	254	243	
T_{100} [°C]	350	266	274	276	270	216
Cetane Number	46	38	46	62	34	70
Lower heating value [MJ/kg]	42.975	43.228	43.2	44.138	42.801	43.33
Density at 15°C [kg/m^3]	843	812	806	755.9	870.2	778.9
C/H mass ratio	6.53	6.19	6.19	5.49	6.58	5.96
Stoichiometric Air/Fuel ratio	14.47	14.62	14.62	14.96	14.46	14.73
Aromatics volume %	27	11	19	0.4	1.9	23
Sulfur [ppm]	9	1	0	0	0	
Kin. Visc. (-20°C) [mm^2/s]	-	4.465	5.2	4.6	7.5	
Kin. Visc. (40°C) [mm^2/s]	2.35	~ 1.4				
Freeze Point [°C]	-	-57	-48	-51	-65	
Flash Point [°C]	73	47	51	45	61	

Tab. 10

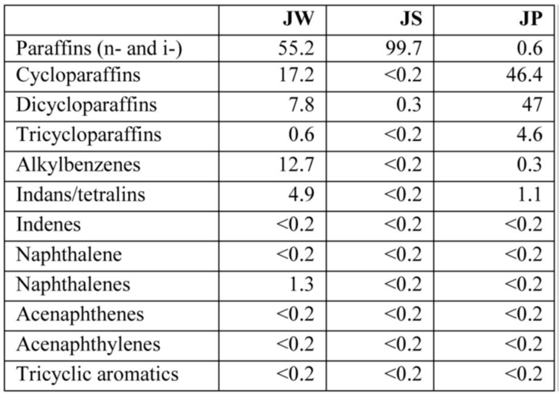

	JW	JS	JP
Paraffins (n- and i-)	55.2	99.7	0.6
Cycloparaffins	17.2	<0.2	46.4
Dicycloparaffins	7.8	0.3	47
Tricycloparaffins	0.6	<0.2	4.6
Alkylbenzenes	12.7	<0.2	0.3
Indans/tetralins	4.9	<0.2	1.1
Indenes	<0.2	<0.2	<0.2
Naphthalene	<0.2	<0.2	<0.2
Naphthalenes	1.3	<0.2	<0.2
Acenaphthenes	<0.2	<0.2	<0.2
Acenaphthylenes	<0.2	<0.2	<0.2
Tricyclic aromatics	<0.2	<0.2	<0.2

Tab. 11

Distillation curve, as for D2 derives from linear interpolation of the three point given and is presented in Fig.6.

Due to the composition of only alkanes (other species are present in neglectable percentages), it's possible to calculate the mean molecular weight starting from the C/H mass ratio. Knowing that a generic alkane has the formula $C_X H_{2X+2}$ and that the C/H mass ratio is 5.49, it's sufficient to solve the following equation to obtain the mean chemical formula:

$$\frac{X \cdot 12}{2X+2} = 5.49 \;\rightarrow X = 10.76$$

The average molecular formula of JS fuel results to be $C_{10.76}H_{23.52}$ and therefore the molecular weight can be adopted as targeted property instead of LHC since alkanes share almost the same value (44.3 MJ/kg).

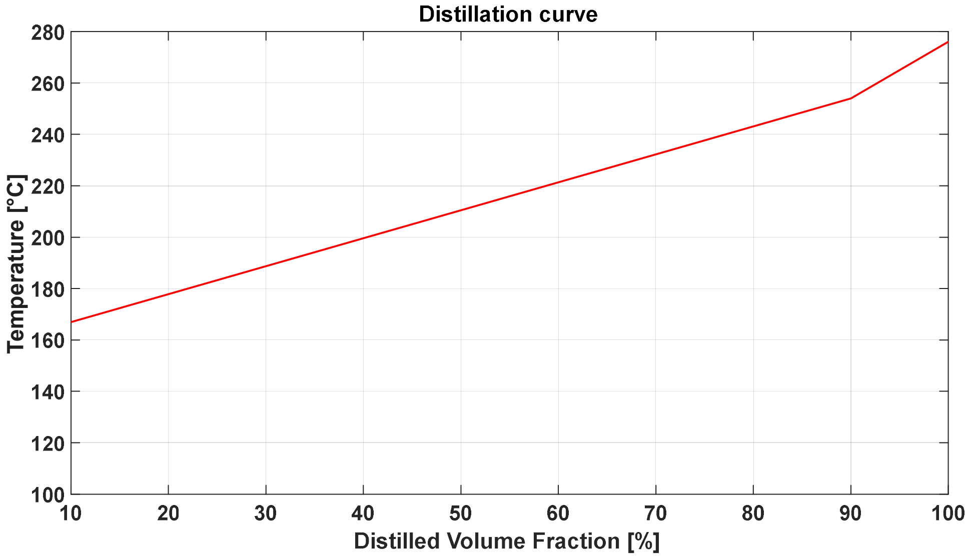

Fig. 18

The composition comprises almost only alkanes: the following components have therefore been chosen as suitable candidates for the surrogate fuel.

2-methyl-heptane	(C_8H_{18} – 2MH)
2-methyl-octane	(C_9H_{20} – 2MO)
2-methyl-nonane	($C_{10}H_{22}$ – 2MN)
Normal-dodecane	($C_{12}H_{26}$ – nC12)
2,2,4,4,6,8,8-heptamethyl-nonane	($C_{16}H_{34}$ – HMN)

The first three have been chosen due to their relatively short carbon chain, in order to keep a C/H mass ratio around 5.5 (JS presents a C/H ratio of 5.49). A linear interpolation has been applied to the distillation curve of JS fuel, in order to evaluate the T_{50}: a value of 210.5 °C lead to choose the n-dodecane as another candidate. The highly branched alkane HMN has been used to reduce the resulting cetane number of the mixture.

Properties of these components are reported in Tab.12, calculated again using the equations given in the Yaws' Handbook [20].

	2MH	**2MO**	**2MN**	**nC12**	**HMN**
CN	49.80	48.70	54.20	74.00	14.70
ρ	703.80	717.66	730.53	751.89	778.25
C/H (mass)	5.338	5.405	5.459	5.543	5.651
MW	114.231	128.258	142.285	170.338	224.446

Tab. 12

Five mixtures, reported in Tab.13, have been investigated: resulting properties for each mixture is reported in Tab.14.

	2MH	2MO	2MN	nC12	HMN
Mix.1	5%	-	-	75%	20%
Mix.2	-	15%	-	70%	15%
Mix.3	-	-	20%	65%	15%
Mix.4	5%	10%	-	70%	15%
Mix.5	5%	-	10%	70%	15%

Tab. 13

	JS	Mix.1	Mix.2	Mix.3	Mix.4	Mix.5
CN	62	60.87	61.31	61.15	61.31	61.86
ρ	755.9	754.76	750	752.64	750.02	751.31
C/H (mass)	5.49	5.55	5.55	5.55	5.53	5.54
MW	~ 153.2	176.37	174.97	173.52	174.13	175.46

Tab. 14

As for traditional diesel, some mixtures results to have 4 components: however the increased precision in matching the targeted properties isn't enough to justify the increase of computational load or to proceed with an approach of generating two different surrogates for the liquid and the gaseous phase and therefore Mix.4 and Mix.5 are rejected. The remaining mixtures presents the almost the same property matching: all of them have a MW higher the target and a cetane number slightly lower. However for the 2-methylheptane an already reduced kinetic mechanism is available, therefore Mix.1 is the one presenting the best trade-off between accuracy in property matching and computational load and so will be implemented in the numerical simulations.

4.6 HVO Surrogate Fuel

Hydrotreated vegetable oil is a new fuel and therefore the available literature covers only a small part of it. However the work of La Puerta et al [29] is a starting point from which HVO properties can be retrieved. Moreover, in that paper a chromatography analysis on the bio-fuel has been performed to analyze the composition of HVO and the results are reported in Tab. 15. The same paper also provides a characterization of hydrotreated vegetable oil and compares it to the traditional diesel fuel (see Tab.16).

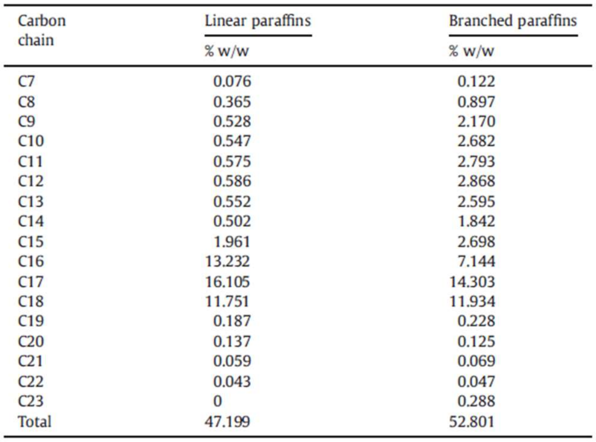

Carbon chain	Linear paraffins	Branched paraffins
	% w/w	% w/w
C7	0.076	0.122
C8	0.365	0.897
C9	0.528	2.170
C10	0.547	2.682
C11	0.575	2.793
C12	0.586	2.868
C13	0.552	2.595
C14	0.502	1.842
C15	1.961	2.698
C16	13.232	7.144
C17	16.105	14.303
C18	11.751	11.934
C19	0.187	0.228
C20	0.137	0.125
C21	0.059	0.069
C22	0.043	0.047
C23	0	0.288
Total	47.199	52.801

Tab. 15

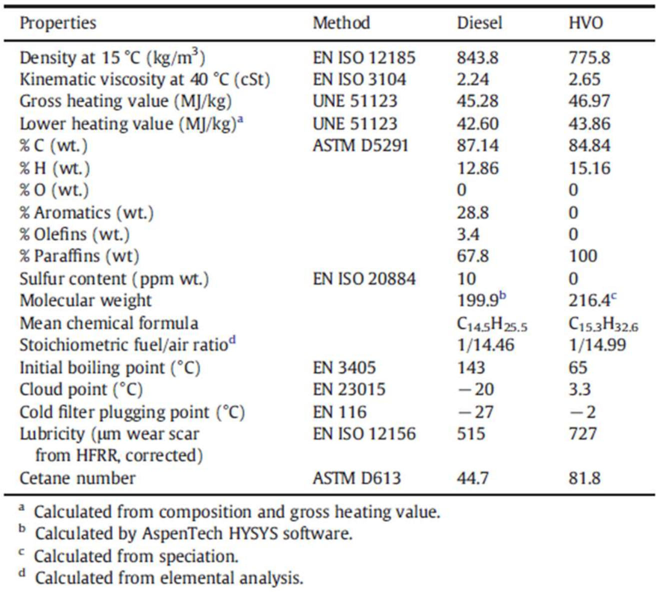

Properties	Method	Diesel	HVO
Density at 15 °C (kg/m^3)	EN ISO 12185	843.8	775.8
Kinematic viscosity at 40 °C (cSt)	EN ISO 3104	2.24	2.65
Gross heating value (MJ/kg)	UNE 51123	45.28	46.97
Lower heating value (MJ/kg)[a]	UNE 51123	42.60	43.86
% C (wt.)	ASTM D5291	87.14	84.84
% H (wt.)		12.86	15.16
% O (wt.)		0	0
% Aromatics (wt.)		28.8	0
% Olefins (wt.)		3.4	0
% Paraffins (wt)		67.8	100
Sulfur content (ppm wt.)	EN ISO 20884	10	0
Molecular weight		199.9[b]	216.4[c]
Mean chemical formula		$C_{14.5}H_{25.5}$	$C_{15.3}H_{32.6}$
Stoichiometric fuel/air ratio[d]		1/14.46	1/14.99
Initial boiling point (°C)	EN 3405	143	65
Cloud point (°C)	EN 23015	−20	3.3
Cold filter plugging point (°C)	EN 116	−27	−2
Lubricity (μm wear scar from HFRR, corrected)	EN ISO 12156	515	727
Cetane number	ASTM D613	44.7	81.8

[a] Calculated from composition and gross heating value.
[b] Calculated by AspenTech HYSYS software.
[c] Calculated from speciation.
[d] Calculated from elemental analysis.

Tab. 16

As for JS fuel, the molecular weight (MW) has been used as target property instead of lower heat of combustion (LHC) due the alkane-only composition. Besides, in this case a value for MW and the average chemical formula are known.

Distillation curve for hydrotreated vegetable oil has also been obtained from the work of La Puerta et al. [29] (Fig.7).

The surrogate candidates have been selected, as for JS fuel, among the alkanes:

Normal-pentadecane	(C15H32, nC15)
2,2,4,4,6,8,8-heptamethyl-nonane	(C16H34, HMN)
2-methyl-pentadecane	(C16H34, 2MP)
2-methyl-heptane	(C8H18, 2MH)

The first three candidates have been selected in order to match the average molecular formula of HVO, $C_{15.3}H_{32.6}$ and thus have C15/C16 carbon chains. The last component has been chosen because of it's low boiling point that allows to match the low temperature distillation of hydrotreated vegetable oil. It should be noticed that although HVO presents a high cetane number, n-pentadecane and 2-methylpentadecane have a CN too high (96.50 and 85.41 respectively). On the contrary the highly branched alkane HMN shows a low value for cetane number (14.70).Moreover, the heptamethylnonane is a fundamental component in diesel-like fuels, so it has been chosen as a candidate for the surrogate mixture.

In Tab.17 the properties for the presented alkanes are reported, while Tab.18 and Tab.19 present, respectively, the proposed mixtures and relative properties.

	2MH	**nC15**	**HMN**	**2MP**
CN	49.80	96.50	14.70	85.41
ρ	703.80	771.79	778.25	773.31
C/H (mass)	5.338	5.630	5.651	5.651
MW	114.231	212.419	226.446	226.446

Tab. 17

	2MH	nC15	HMN	2MP
Mix.A	0	0.81	0.19	0
Mix.B	0	0.68	0.16	0.16
Mix.C	0.09	0.75	0.16	0

Tab. 18

Please notice that mixture compositions are given in terms of volume fractions

	HVO	Mix.A	Mix.B	Mix.C
CN	81.8	81.09	81.89	79.13
ρ	775.80	773.01	773.05	766.4
C/H (mass)	5.59	5.634	5.636	5.581
MW	216.4	219.94	216.63	199.79

Tab. 19

As Fig.7 shows, the distillation points of Mix.C matches more the distillation curve for hydrotreated vegetable oil given by La Puerta et al [29]. Mix.B, on the other hand, matches the HVO properties with more accuracy. Again, the computational load parameter is used as control parameter and the availability of an already reduced kinetic mechanism for the oxidation of 2-methylheptane has led to the selection of Mix.C as surrogate for hydrotreated vegetable oil.

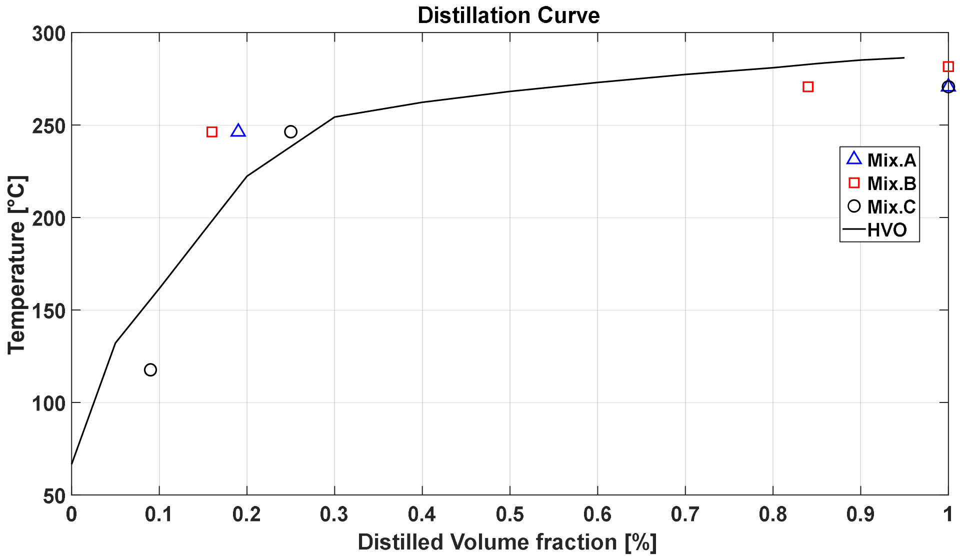

Fig. 19

As the CONFVERGE CFD software requires different properties to simulate the fuel and many of them are temperature dependant, a more precise characterization of the target fuel allows to generate a surrogate that better mimics the spray and combustion related properties. Therefore the model will be more consistent and robust because the surrogate fuel will mimic the target fuel properties not only at a single temperature but over a range of temperature. If we take in exam the HVO surrogate, in fact, it can be noticed how the investigated mixtures have a different behaviour at different temperatures, as shown in Fig. 7-9. Having known the values of the properties at different temperature would have ensured a more accurate surrogate fuel.

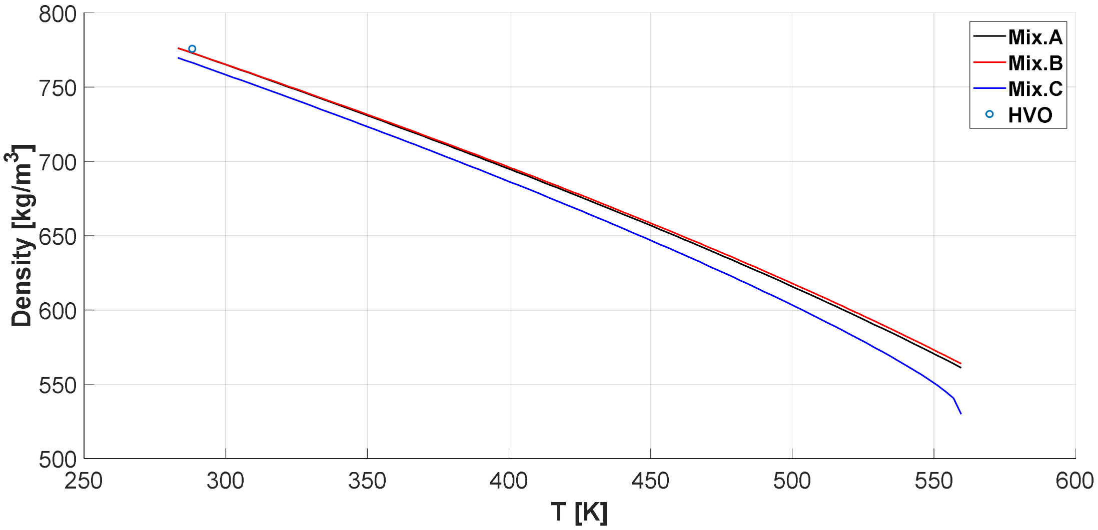

Fig. 7 – Density

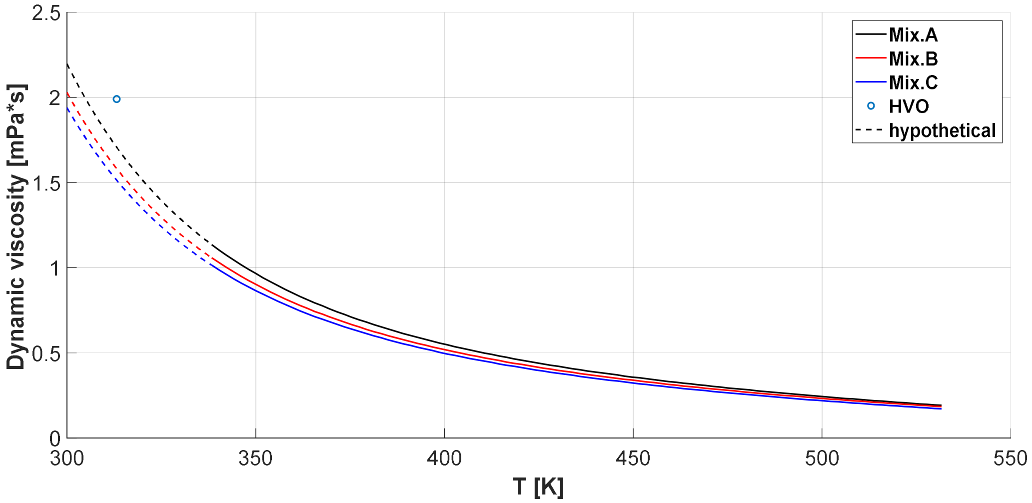

Fig. 8 – Viscosity

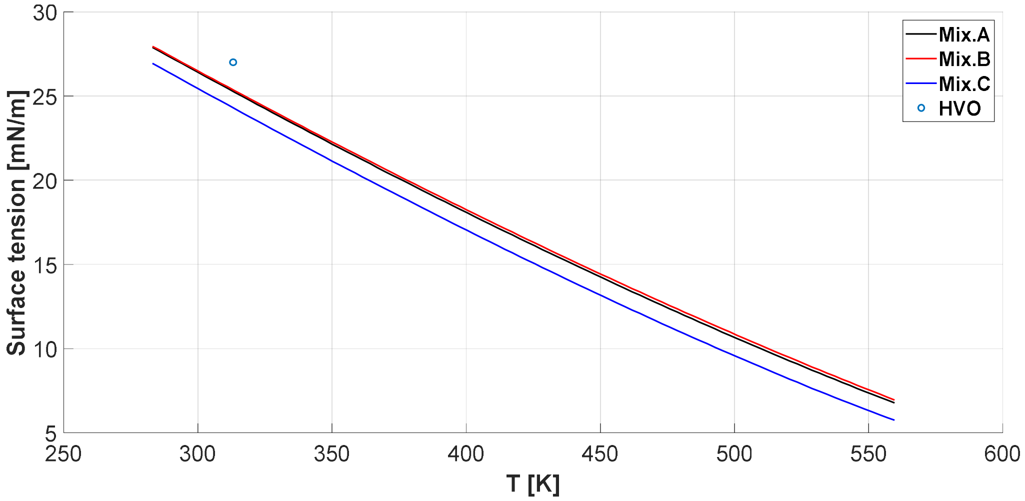

Fig. 9 – Surface Tension

5 SPRAY INJECTION SIMULATIONS

5.1 The experimental data

The Engine Combustion Network collaborates with numerous institutions, like the Sandia National Laboratories, the Argonne National Laboratory and the CMT-Motores Termicos, to collect and share experimental data, diagnostics and computational results.[34]

The diesel combustion is tested in a precisely defined vessel (constant volume combustion) and a wide range of conditions, usually experienced in diesel engines, can be simulated:

- Ambient gas temperatures from 450 K to 1300 K
- Ambient gas densities from 3 to 60 kg/m3
- Ambient gas oxygen concentrations from 0% to 21%

The vessel, as reported in Fig.1, has a cubical-shaped combustion chamber. Each side of the vessel has a round port with a diameter of 105 mm. The fuel injector is located in one side port using a metal insert that forms the side wall. Another metal insert forms the top wall of the chamber, where a fan and two spark plugs are mounted. The remaining sides of the vessel present four optical access with apertures of 102 mm. Intake and exhaust valves, or instruments such as pressure transducers or thermocouple inputs, are mounted at the corners of the cubical-shaped combustion chamber. Fig.2 and Fig.3 reports the internal view and a schematic section respectively.

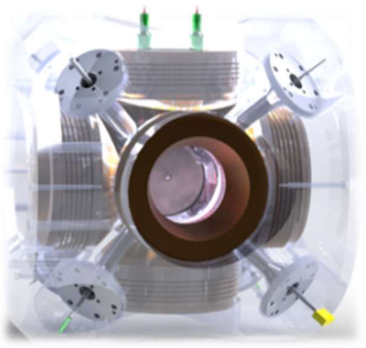

Fig. 1

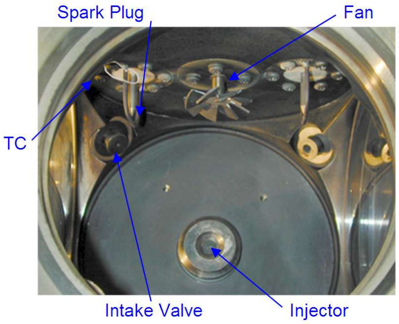

Fig.2

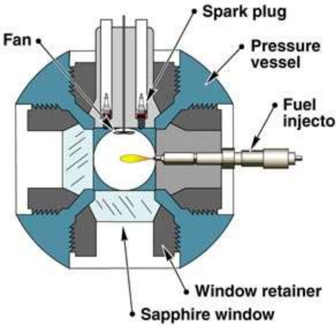

Fig. 3

The two spark plug provide consistent combustion in the high-density, fuel-lean ambient, while the mixing fan is used to ensure uniformity in ambient conditions. In 2009 the Sandia vessel has been updated: the fan has been moved to the top side corner and its rotation where lowered from 8000rpm to 1000 rpm in order to reduce optical interferences and thermal boundary layer on the windows.

The ECN working group identified a set of experimental conditions called “Spray A”, for single-hole nozzle, and “Spray B”, for three-hole nozzle. Beginning in 2007, at Sandia National Laboratories spray experiments were performed with a Bosch Generation-2 common rail fuel injector equipped with different single-hole axial nozzles.

Spray A condition is a low-temperature combustion condition that is usually encountered in diesel engines with a moderate EGR. Detailed specifications for Spray A conditions are reported in Tab.1.

Specifications for Spray A operating condition of the Engine Combustion Network[a]	
Ambient gas temperature	900 K
Ambient gas pressure[b]	near 6.0 MPa
Ambient gas density[b]	22.8 kg/m^3
Ambient gas oxygen (by volume)	15% O2 (reacting); 0% O2 (non-reacting)
Ambient gas velocity	Near-quiescent, less than 1 m/s
Common rail fuel injector	Bosch solenoid-activated, generation 2.4
Fuel injector nominal nozzle outlet diameter	0.090 mm
Nozzle K factor	K = (dinlet – doutlet)/10 [use µm] = 1.5
Nozzle shaping	Hydro-eroded
Mini-sac volume	0.2 mm^3
Discharge coefficient	C_d = 0.86, 10 MPa pressure drop and diesel fuel
Number of holes	1 (single hole)
Orifice orientation	Axial (0&deg full included angle)
Fuel injection pressure	150 MPa (1500 bar), prior to start of injection
Fuel	n-dodecane[c]
Fuel temperature at nozzle[d]	363 K (90°C)
Common rail[e]	GM Part number 97303659. Used by 2005-2006 Duramax engines.
Common rail volume/length	22 cm^3/28 cm
Distance from injector inlet to common rail	24 cm
Tubing inside and outside diameters[f]	Inside: 2.4 mm. Outside: 6-6.4 mm.
Fuel pressure measurement	7 cm from injector inlet / 24 cm from nozzle
Injection duration	1.5 ms
Injection mass	3.5 – 3.7 mg
Approximate injector driver current	18 A for 0.45 ms ramp, 12 A for 0.345 ms hold

Tab. 1

[a] from SAE Paper 2010-01-2106

[b] This exact combination of ambient pressure and density corresponds to a particular set of gases for a 0%-O2 condition with 89.71% N2, 6.52% CO2, and 3.77% H2O by volume and a compressibility factor, Z = 1.01. When different gases are used, the pressure must vary to maintain the same density

[c] Chosen as a fluorescence-free diagnostics fuel with known chemistry and properties. Other fuels may be selected after initial study and comparison.

[d] Measured upstream of the orifice, at the time that injection would take place, see SAE Paper 2010-01-2106. May be slightly different than injector body temperature, and different than the steady state temperature.

[e] Use rail outlet farthest away from fuel entrance (small orifice) to rail (i.e. cylinder #1).

[f] This 24 cm tube is available for purchase from USUI, reference part number IFP1. It is rated for 2500 bar.

Having a full optical access, different experimental diagnostic are available and used: schlieren imaging, mie-scattering and laser extinction can be used for vapor and liquid penetration. Ignition delay and lift-off length are evaluated as well with a light-based model that measure the chemiluminescence.

5.2 Spray break-up model calibration and mesh limitations

Since the spray sub-models are generally grid-dependent, an analysis on the mesh size influence has been made. Generally, a fine grid can reproduce better the experimental results than a coarse grid, but with higher computational costs: thus a trade-off has to be found. Moreover the spray break-up model will also be calibrated in terms of shed factor, one of the many coefficients that CONVERGE allows to be user defined. It should be remembered, however, that the standard coefficients provided by the software are well established and validated for a range of cases and conditions.

The CONVERGE Advanced Training material suggest to perform the mesh dependency analysis comparing different quantities in different conditions:

NON-EVAPORATING CONDITIONS	EVAPORATING CONDITIONS	COMBUSTING CONDITIONS
Axial velocity Turbulent kinetic energy Turbulent length-scale Turbulent viscosity Liquid and vapor penetration Mixture fraction	Liquid penetration Vapor penetration	Ignition delay Lift-off length

Non-evaporating conditions consist of an ambient composed of sulphur hexafluoride (SF_6) at low temperature (298 K) and density comparable con the other conditions (22 kg/m^3). The evaporating conditions are the same of the non-reacting simulations, therefore with an ambient with 0% of O_2 at a temperature that allows evaporation (900 K) and a density comparable to the diesel engine applications (22.8 kg/m^3). Finally, reacting conditions presents an ambient at 22.8 kg/m^3, temperature of 800÷1300 K and an oxygen content ranging from 10% to 21%: the variable O_2% represents the presence of EGR.

Due to limitations in available computational power, only the non-reacting and the reacting conditions were analysed.

5.2.1 Non-reacting case

The analysis has been made through 4 simulations, in conditions listed in the table below

	Simulation A	Simulation B	Simulation C	Simulation D
Fuel	nC12			
Nozzle	Spray A, nozzle hole= 0.0837mm, single hole injector			
Ambient conditions	Temp = 900K ρ = 22.8kg/m^3 Press = 6.09Mpa N2 = 87% O2=0% CO2=6.53% H2O = 3.77% [mol_frac]	Temp = 900K ρ = 22.8kg/m^3 Press = 6.09Mpa N2 = 87% O2=0% CO2=6.53% H2O = 3.77% [mol_frac]	Temp = 900K ρ = 22.8kg/m^3 Press = 6.09Mpa N2 = 75.15% O2=15% CO2=6.22% H2O = 3.62% [mol_frac]	Temp = 900K ρ = 22.8kg/m^3 Press = 6.09Mpa N2 = 75.15% O2=15% CO2=6.22% H2O = 3.62% [mol_frac]
Injection Conditions	Injection Pressure = 150Mpa, Injection duration = 6.09ms, Cd= 0.89			
Fuel conditions	Temp = 363K			
Embed scale	3	4	5	5
KH Shed Factor	0.1	0.1	0.2	0.1

Tab. 2

The embed scale parameters defines the embedded mesh size as defined:

$$d_{x\_embed} = \frac{d_{x\_base}}{2^{embed\_scale}}$$

Since $d_{x\_base} = 4mm$:

- Simulation A -> 0.500 mm
- Simulation B -> 0.250 mm
- Simulation C -> 0.125 mm
- Simulation D -> 0.125 mm

The liquid penetration is calculated from numerical results as the distance within a certain percentage of the injected mass is located: usually a value of 97% is chosen in order to avoid miscalculation due to approximations of the model. In fact it can be noticed how considering the 99% of the mass leads to a substantial overprediction since also the smallest, furthest from injector parcels are considered.

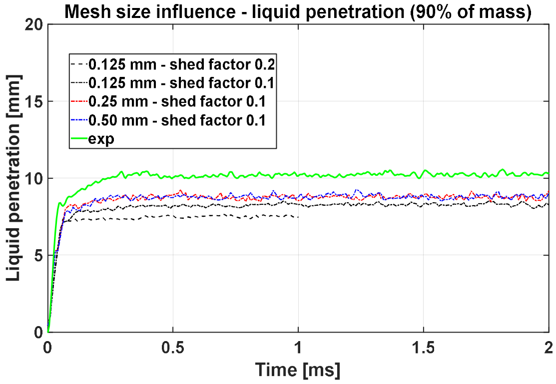

Fig. 1

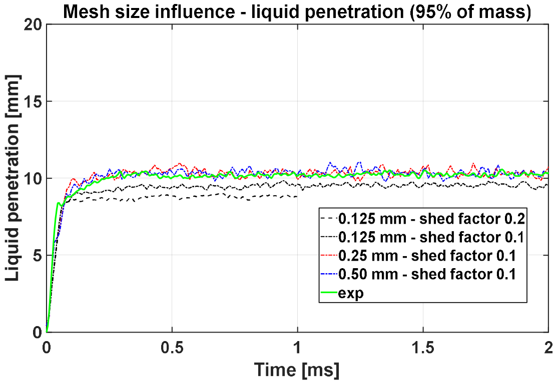

Fig. 2

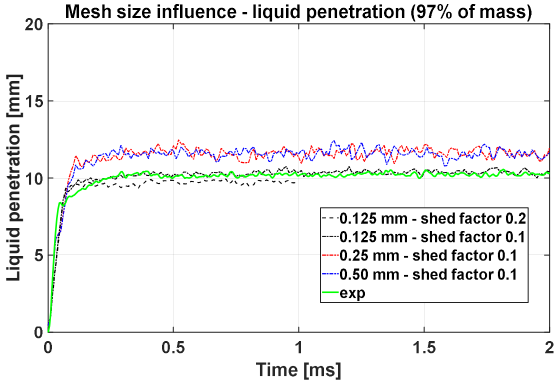

Fig. 3

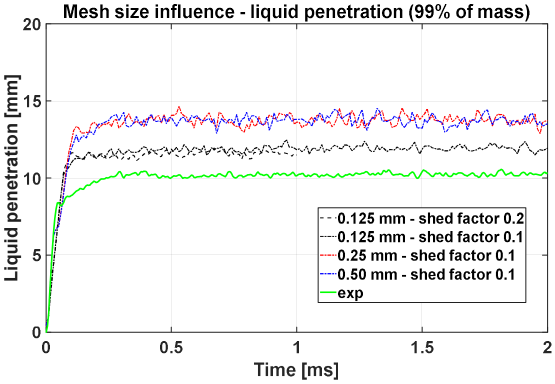

Fig. 4

It's evident that a 0.125 mm mesh allows a better precision in the simulations: the calculated liquid penetration, in fact, is closer to the experimental one. The shed factor, as mentioned above, has an effect on the Sauter Mean Diameter and thus on the liquid penetration: however, as it can be noticed, this influence is minimal.

Regarding the vapor penetration, results shown in Fig.5 have been obtained:

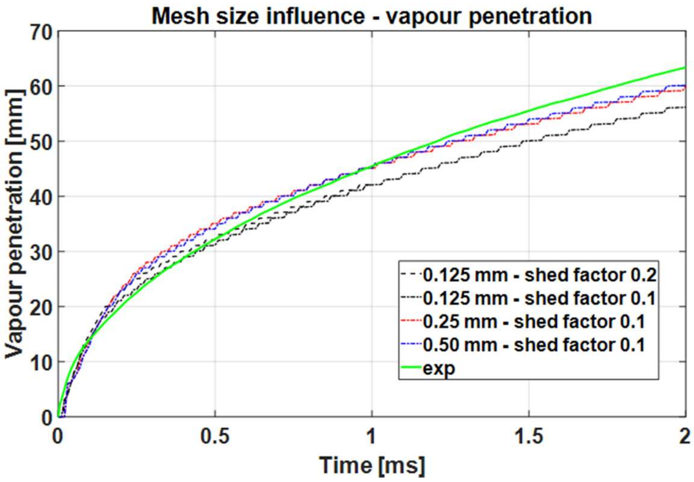

Fig. 5

It can be noticed how the numerical data from finer mesh fit better the experimental ones in the first stages of injection. Vice versa, a more coarse grid reduces the underprediction in the last moments but increases the overprediction in the first ones. Again, the shed factor influence is minimal and it will be investigated better with the analysis of the reacting case.

It has been noticed, moreover, that the reduced liquid penetration using coarse grids is probably due to increased radial diffusion of the droplets, while finer grids tend to better simulate the axial distribution.

5.2.2 Reacting case

Due to the excessive computational load to run a combustion simulation with a mesh size of 0.125 mm, the analysis has been limited to the influence of the shed factor, as reported in the table below, adopting a mesh size of 0.25mm.

	Case 1	**Case 2**
Fuel	nC12, JS	
Nozzle	Spray A, nozzle hole= 0.0837mm, single hole injector	
Ambient conditions	Temp = 900K density = 22.8kg/m^3 Pressure = 6.09Mpa N2 = 87% O2=0% CO2=6.53% H2O = 3.77% [mol_frac]	Temp = 900K density = 22.8kg/m^3 Pressure = 6.09Mpa N2 = 75.15% O2=15% CO2=6.22% H2O = 3.62% [mol_frac]
Mesh size	0.5,0.25,0.125 [mm]	0.25 [mm]
Model settings	KH shed-factor = 0.1	KH shed-factor = 0.2
Injection Conditions	Injection Pressure = 150Mpa, Injection duration = 6.09ms, Cd= 0.89	
Fuel conditions	Temp = 363K	

Tab. 3

As mentioned before, in the reacting case the parameters analyzed and compared are the ignition delay and location and the lift-off length.

In Fig.6 the ignition delay and the ignition location from experimental data are compared to the results from numerical simulations. The experimental data are obtained using a high-speed camera. Using an image processing, temperature is estimated from luminosity: after quantifying the maximum level of luminosity intensity a threshold of 50% is imposed to define the ignition region. In the experimental data images blue border is 50% of high-temperature chemiluminescence threshold. With the same approach, ignition delay and location has been defined in numerical results as function of temperature. It can be easily noticed how the results from simulation adopting a shed factor of 0.1 are matching better the experimental data.

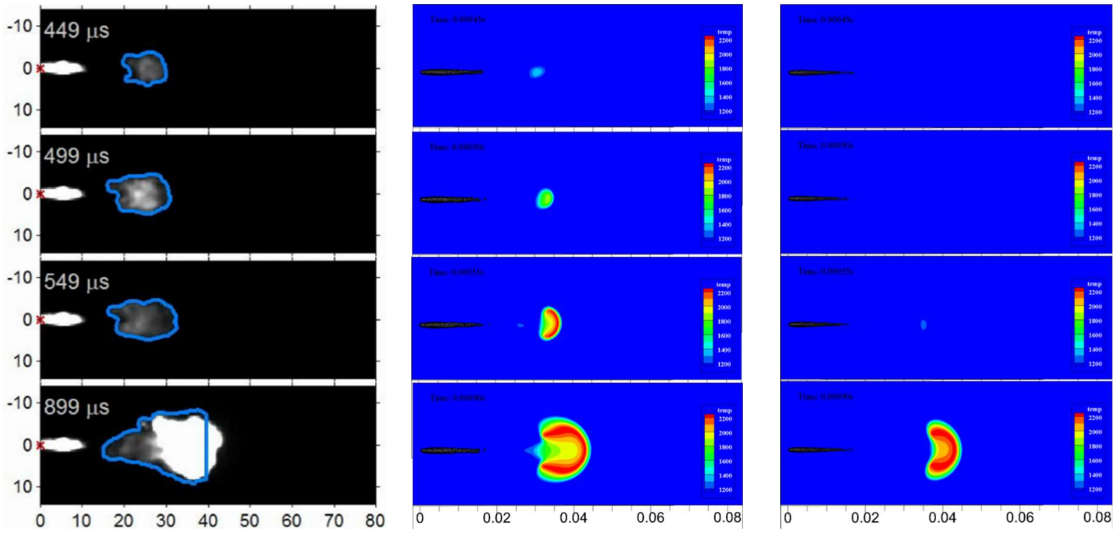

1 – Experimental data

2 – Numerical data

Shed factor = 0.1

3 – Numerical data

Shed factor = 0.2

Fig. 6

Adopting a shed factor of 0.1 and a mesh size of 0.25 mm also results in a good match of the experimental data of the lift-off length, as reported in the following figures.

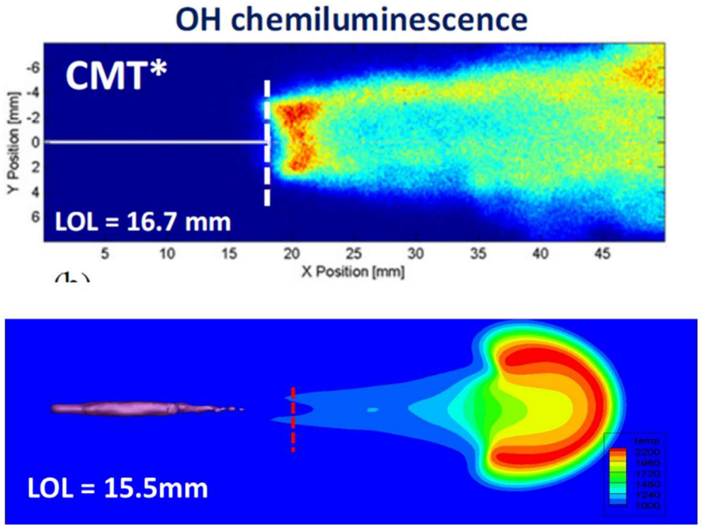

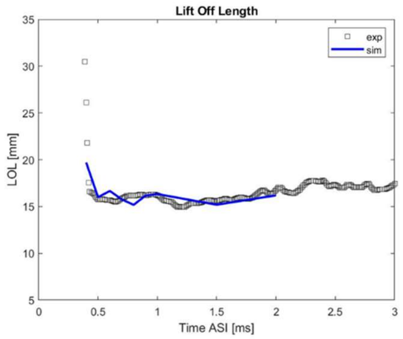

To further validate the model, the ignition delay has been calculated at higher temperature (1000 K) and also adopting the JS surrogate fuel, considering both a temperature of 900 K and 1000 K: the results are presented in Fig.7. In both cases, ignition delay calculated at lower temperature is correct with a maximum error of 0.12 ms. At 1000 K, however, the ignition delay resulting from the numerical simulation where a shed factor of 0.2 has been adopted (case 2) is wrong.

With a certain level of confidence it has been therefore established that the simulations will be run with a mesh size of 0.25 mm and a shed factor for the KH model of 0.1.

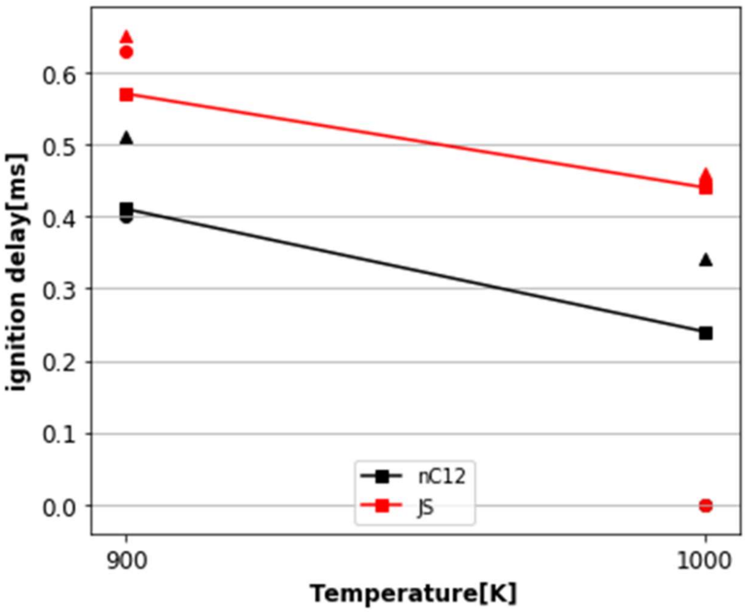

△ Experimental data – case 1

○ Experimental data – case 2

☐ Numerical data

Fig. 7

5.3 Diesel simulations

As said in the surrogate formulation section, Diesel has been simulated adopting a phase separation approach due to its complexity and therefore two surrogates, one for the liquid and one for the gas phase, have been proposed.

The non-reacting case validation compares the numerical and the experimental results of the liquid and vapor penetration: as presented in Fig.1, the accuracy is rather goo

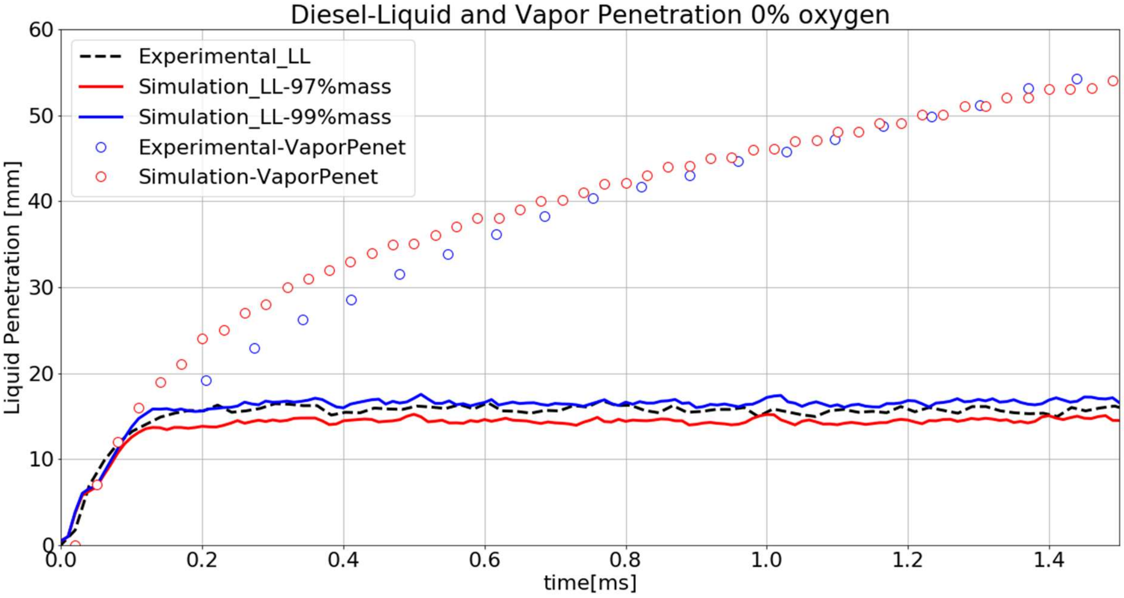

Fig. 1

It can be seen that considering the liquid penetration as the axial length within the 97% of the injected mass is located (Simulation_LL-97%mass) leads to a small underprediction, while calculating it using the 99% of the mass results in an almost perfect match of the results. As always, the vapor penetration is underpredicted in the first moments of the injection while it tends to be overestimated in the late part.

It should be noticed that the injection duration is over 6 ms: here a smaller time window is presented, considering the first time steps as the fundamental ones to validate the model, since it's where the spray injection develops.

The next simulation has been performed in reacting conditions: to simulate the EGR conditions, which are typical in diesel-engines, a 15% O_2 in volume has been considered. Results are compared in terms of ignition delay, ignition location and lift-off length.

Ignition delay numerical and experimental results are presented in Fig.2 and Fig.3 adopting ambient temperature of 900 K and 1000 K respectively. It has been calculated considering a maximum temperature of 1100 K as indication of the start of combustion. As summarized in Tab.1, there's a small overprediction, order of 0.5 ms, in the numerical results: this is due to the mechanism reduction procedure. In fact adopting a reduced kinetic mechanism for oxidation instead of a detailed one, introduces a small approximation.

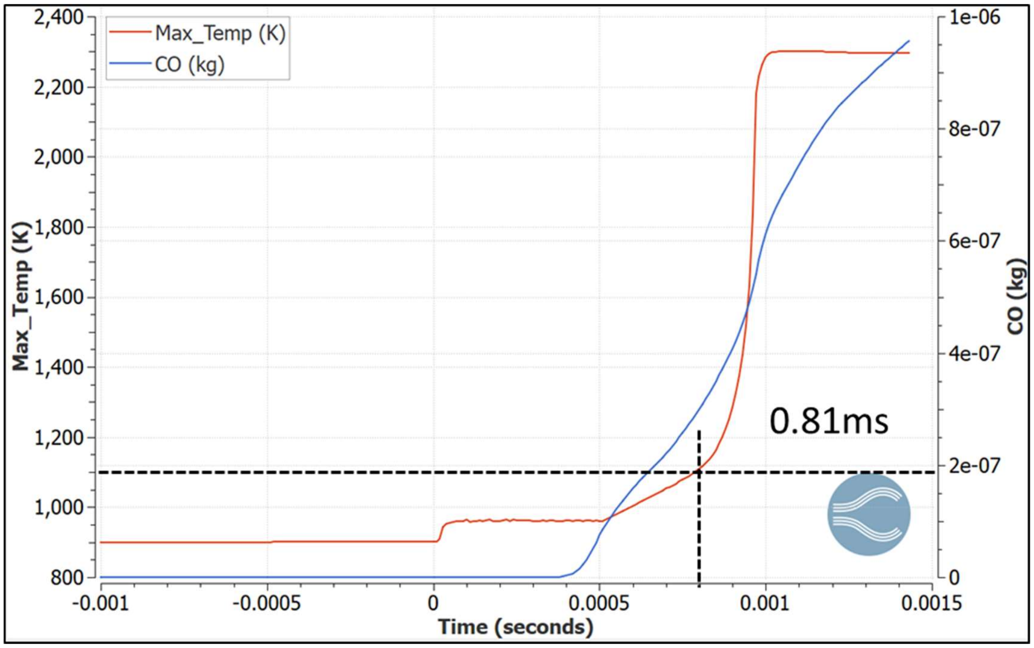

Fig. 2 – Diesel ignition delay at 900 K

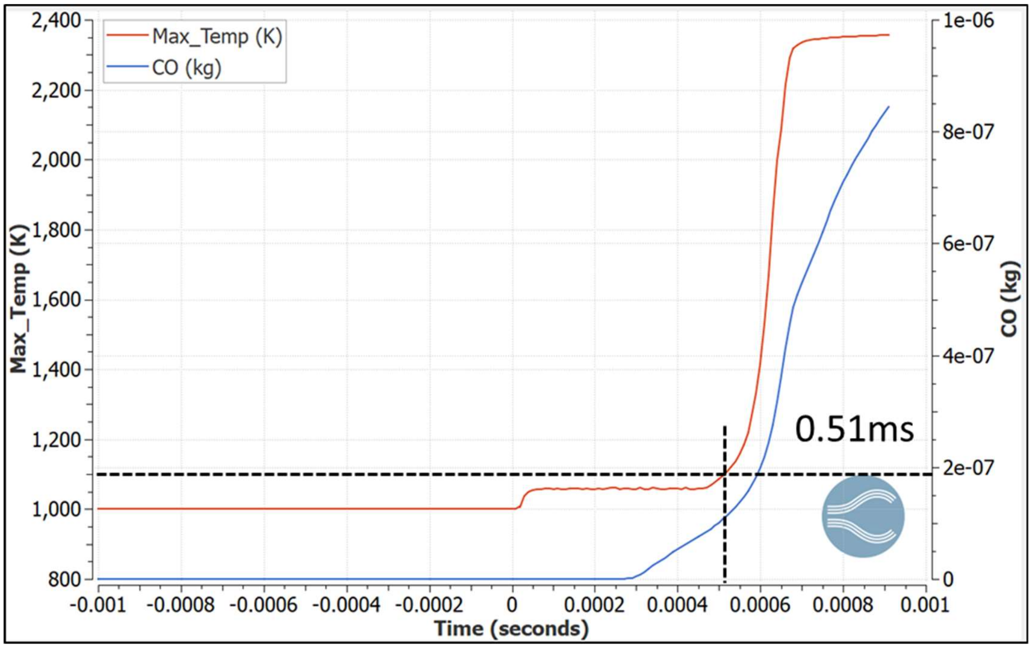

Fig. 3 – Diesel ignition delay at 1000 K

Temperature [K]	Ignition delay ECN (ms)	Ignition delay Numerical (ms)
900	0.77	0.81
1000	0.44	0.51

Tab. 1 – Diesel ignition delay, experimental vs numerical data

In Fig.4 and Fig.5, the numerical temperature evolution and the resulting ignition location are reported and compared with spray injection experimental data acquired using a mie-scatter imaging process:

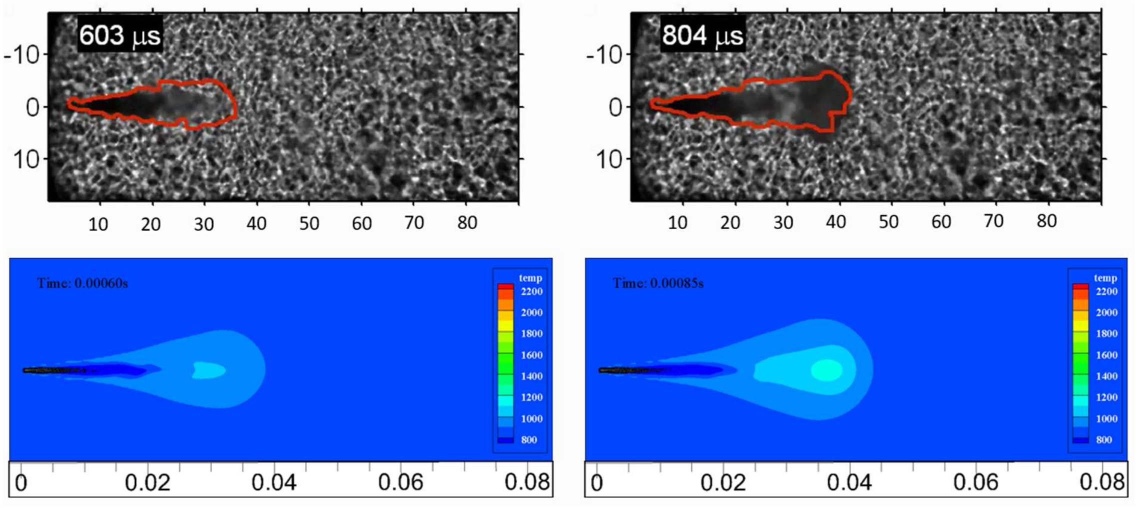

Fig. 4 – Temperature evolution at 0.6 ms (left) and 0.8 ms (right)

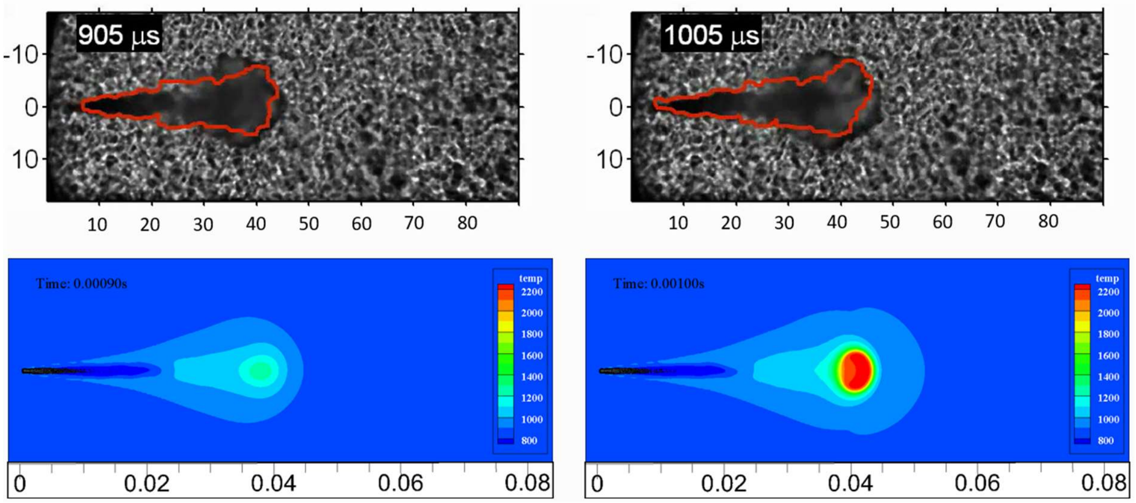

Fig. 5 – Temperature evolution at 0.9 ms (left) and 1.0 ms (right)

It can be noticed also in this case, an overall good matching between the experimental data and the numerical ones. Also, this comparison shows that the spray evolution is matched with a small overprediction: at 1.0 ms, i.e., the numerical results shows spray at an axial distance of around 52 mm, while for the experimental data it's around 49 mm.

Finally the lift-off length, so the axial location where the diffusion flames develop, is analysed: in the experimental data, as mentioned before, it's estimated through the chemiluminescence from OH* radicals. In the numerical simulations, instead, the lift-off length has been estimated considering a temperature increase of a 100K.

Results with ambient temperature of 900 K and 1000 K are reported in Fig.6 and Fig.7 respectively and a noticeable overestimation can be observed: although it's quite common, future investigation and analysis should be performed to understand precisely this behaviour. Probably, however, this significant approximation is probably due to the separated gas phases used due Diesel complexity.

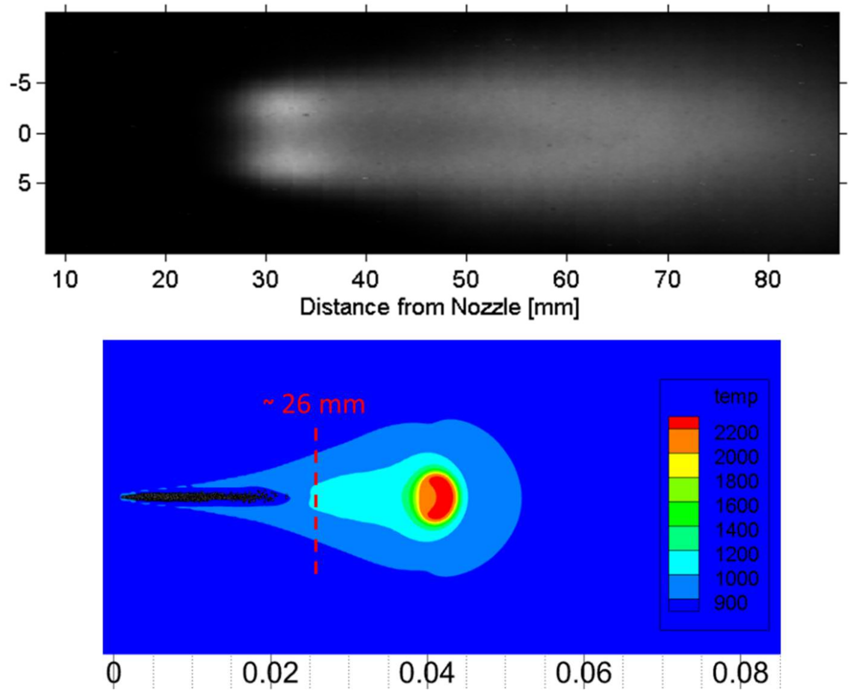

Fig. 6 – Lift-off Length at 900 K

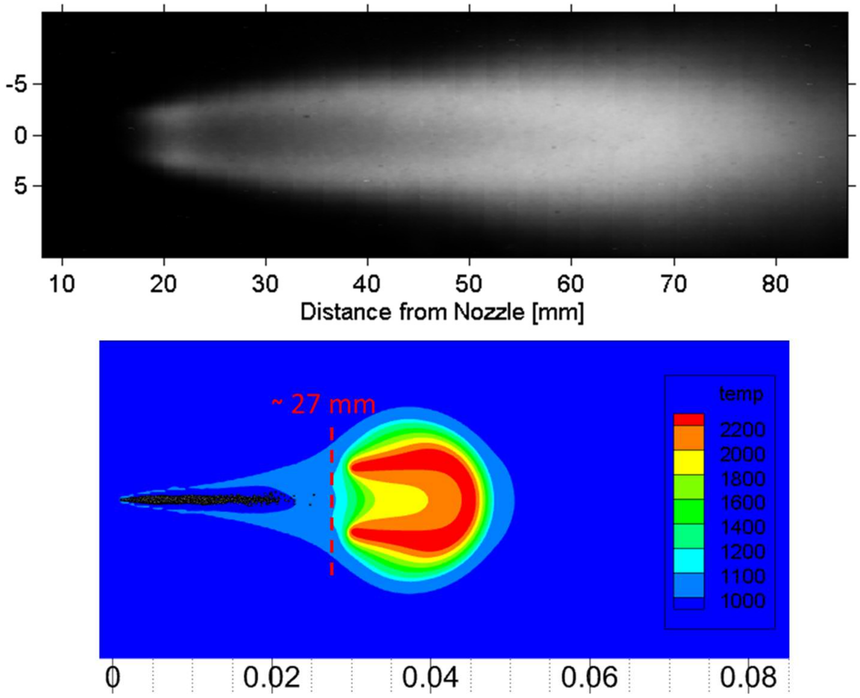

Fig. 7 – Lift-off Length at 1000 K

5.4 JS Fuel simulations

As for Diesel, the first simulation has been run in non-reacting conditions, to obtain numerical results of liquid and vapor penetration. Fig.1 reports the comparison between experimental data and numerical results.

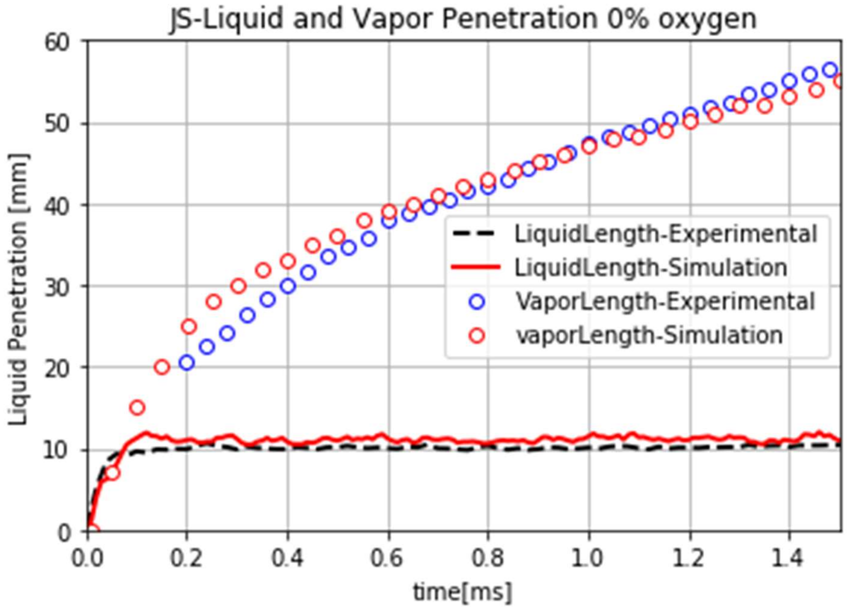

Fig. 1

As anticipated in the Diesel results section, it can be noticed an initial overprediction of vapor penetration, followed by and underestimation of it. The calculated liquid penetration matches the experimental data quite precisely: the initial overestimation is due to an approximation caused by the chosen time-step. A further reduction of the time discretization in the first period of injection, however, would have resulted in a higher computational load and since it’s almost neglectable and at steady state conditions there’s almost no difference between calculated and measured liquid length it has been decided to accept this favorable trade-off.

Following simulations were run in reacting conditions. Again EGR conditions has been simulated and thus the air composition is with O_2 in 15% (in volume). The ignition delay results, as anticipated in the model calibration section, are matching the experimental results within a 0.12 ms error band:

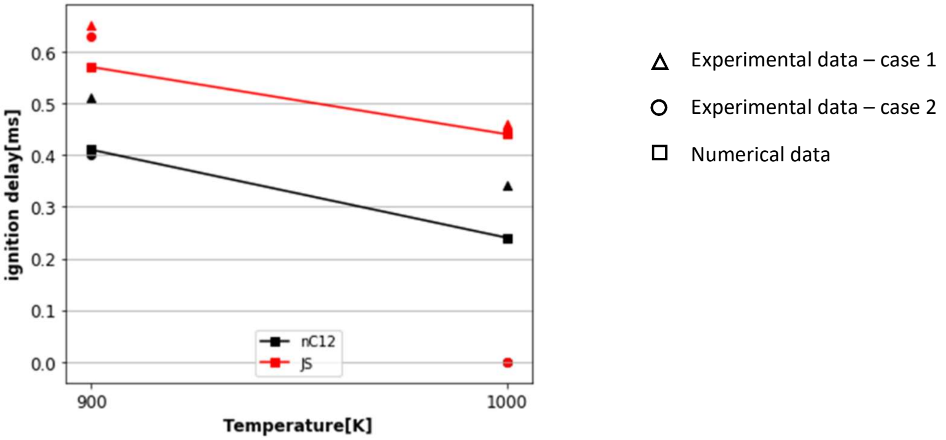

As for Diesel, the calculated lift-off length presents an overestimation with respect to the measured one. In Fig.2 results for two different temperature values are reported: it can be noticed, moreover, how the calculated lift-off length seems to be less dependent on ambient temperature.

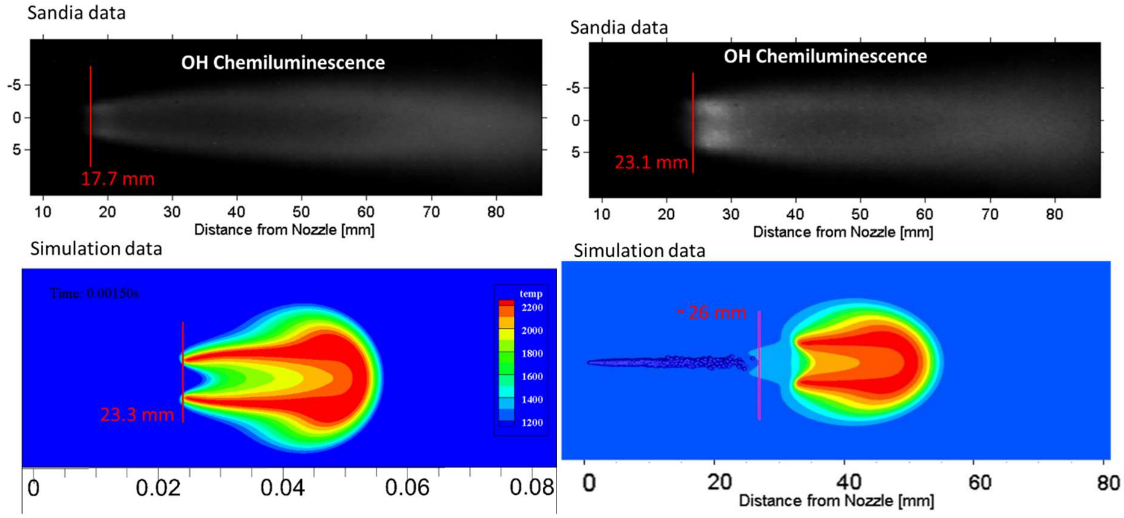

Fig. 2 – Lift-off Length at 900 K (left) and at 1000 K (right)

As shown in Fig.3a, calculated lift-off length presents an initial variation followed by a steady-state condition: this is true also in the real experiment conditions, but the ECN platform reports only an average value for JS. Fig.3b, which reports results for n-dodecane, shows that measuring lift-off length variation also leads to variable values.

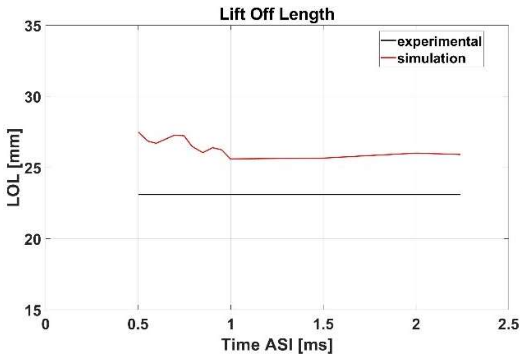

Fig. 3a – Lift-off Length for JS Fuel (900 K)

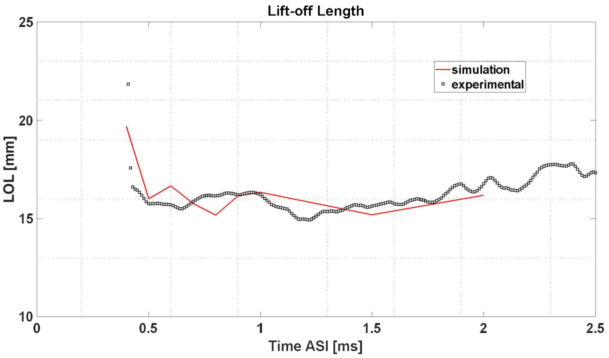

Fig. 3b – Lift-off Length for nC12 (900 K)

A further analysis on the numerical results obtained from JS fuel simulation has been made using the mie-scatter images experimentally obtained: this allowed to compare the spray evolution. Results are presented in Fig.4

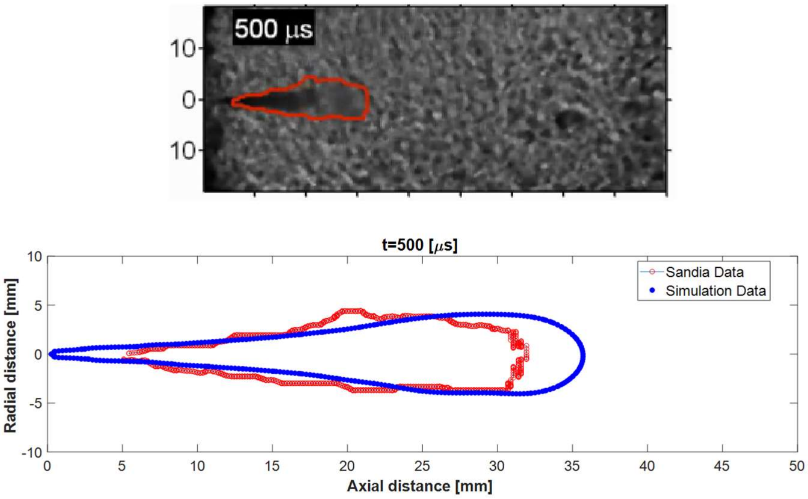

Fig. 4a – JS spray distribution at 0.5 ms

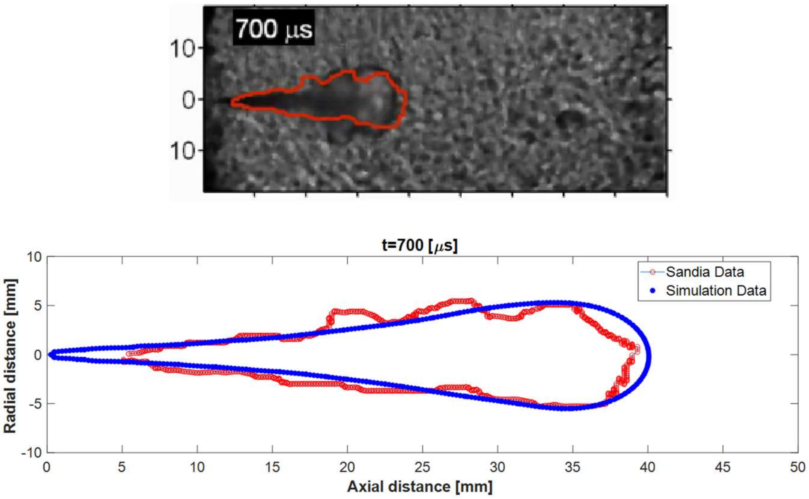

Fig. 4b– JS spray distribution at 0.5 ms

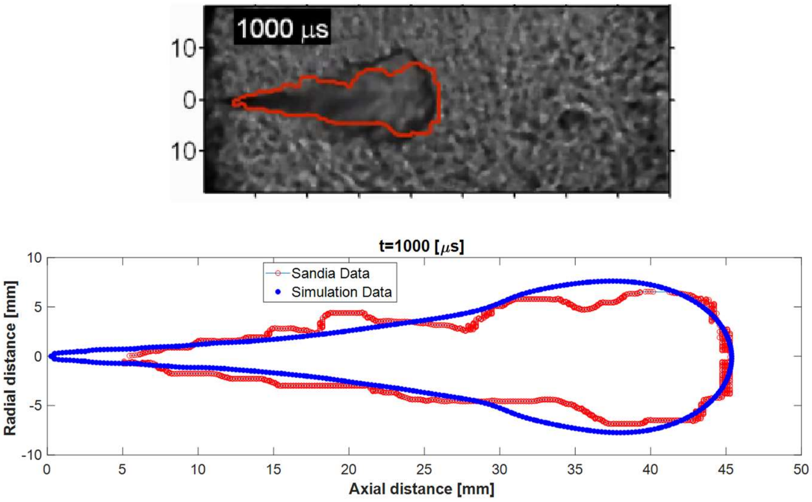

Fig. 4c– JS spray distribution at 0.5 ms

Again, apart from a small initial overestimation the numerical results are matching the experimental data and thus the model is thought to work properly.

For JS Fuel the analysis of emissions is implemented in the model. Results for soot are reported in Fig.5.

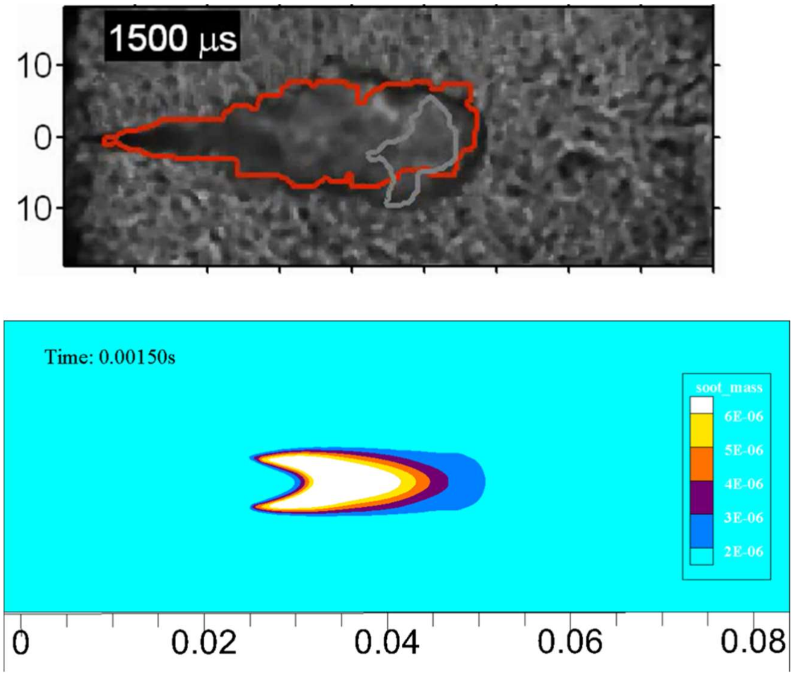

Fig. 5

Unfortunately, the only available experimental data for particulate matter precursor, derives from the mie-scatter images where soot formation region is represented with a grey line and thus, apart from formation region, no other information are available.[34]

The particulate matter (PM) emissions have therefore been investigated with more detail with the comparison between experimental data and numerical results with n-dodecane as fuel. In this case the available experimental data reported also the soot volume formation: this has been estimated experimentally using laser extinction and planar laser-induced incandescence (PLII). Therefore the soot volume is related to the soot optical thickness, KL (where K is the extinction coefficient and L is the path length through the soot), which is in turn estimated from the laser intensities.

The acquiring system and the experimental diagnostic are quite complex and still, the obtained results are an estimation of the soot formation: therefore it isn't surprising that the numerical model to calculate the soot formation isn't matching the experimental data. However a qualitative analysis shows that the model seems to be right. Moreover the model predicts with a rather good accuracy the region where PM precursors begin to generate. Results are reported in Fig.6.

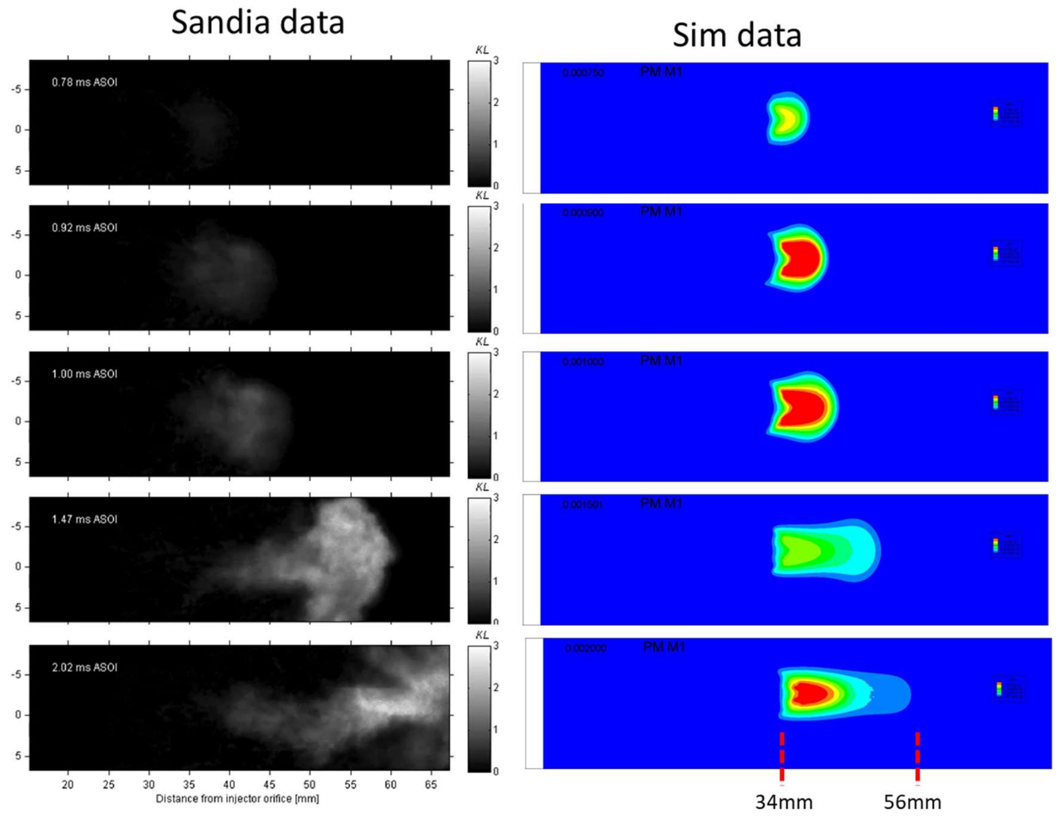

Fig. 6 – Soot formation for nC12

5.5 HVO simulations

As both the defined surrogate approach and the spray injection model have been validated against experimental data, the HVO simulations results are accepted with a high level of confidence and therefore the comparison with Diesel results has been performed.

Again, the first step has been the analysis of the spray characteristics in non-reacting conditions: in Fig.1a the liquid penetration of HVO and diesel are reported (for the second one, both experimental and numerical data).

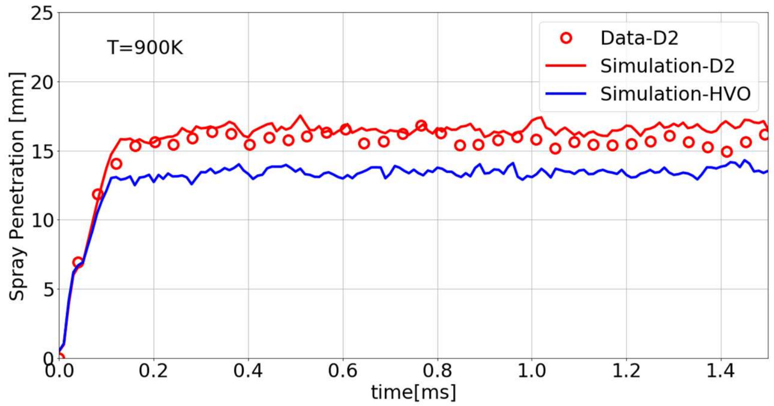

Fig. 1a – Liquid penetration

Vapor penetration is reported in Fig.1b:

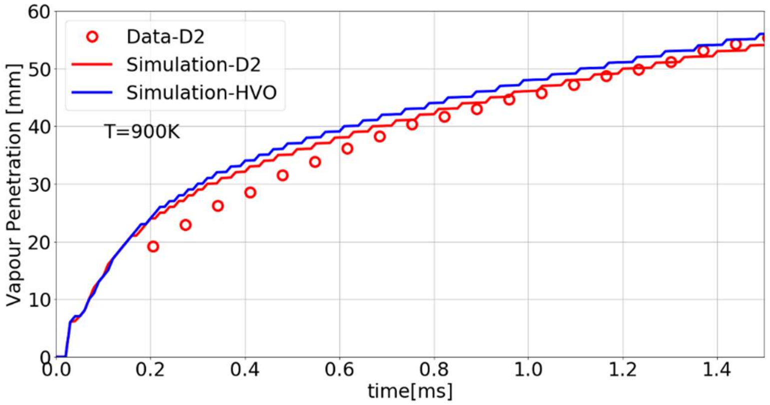

Fig. 1b – Vapor penetration

It can be easily noticed that the hydrotreated vegetable oil presents a -hypothesized- vapor penetration almost identical to that of diesel, while the liquid penetration is quite lower: a first advantage is then already highlighted, since a lower liquid penetration means a lower risk o wall wetting during the injection. Of course this has to be investigated deeper both in engine testing and simulations.

In reacting conditions, again with 15% O_2 in volume, the ignition delay has been calculated both with ambient temperature of 900 K and 1000 K. The results have been reported in Fig.2, where they are compared with different diesel-like fuels.

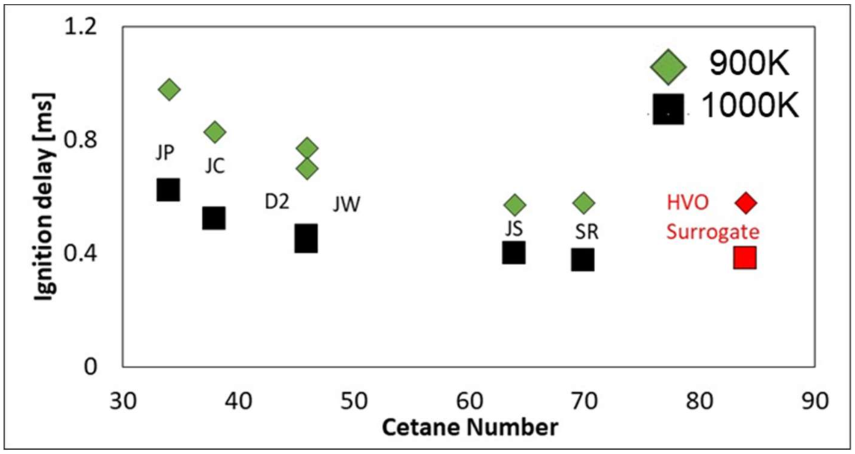

Fig. 2 – Ignition delay

The different fuels ignition delays are obtained from available literature [ref “kook”] and are also reported as function of the cetane number: it can be noticed that the HVO surrogate is in line with the decreasing trend of ignition delay. As the temperature or the cetane number increase, in fact, the ignition delay of the fuel shortens.

It’s interesting to observe that HVO surrogate presents an ignition delay almost equal to that of JS fuel: the similar composition, of pure alkanes, may be the reason for this.

The same comparison has been made for the lift-off length, as reported in Fig.3.

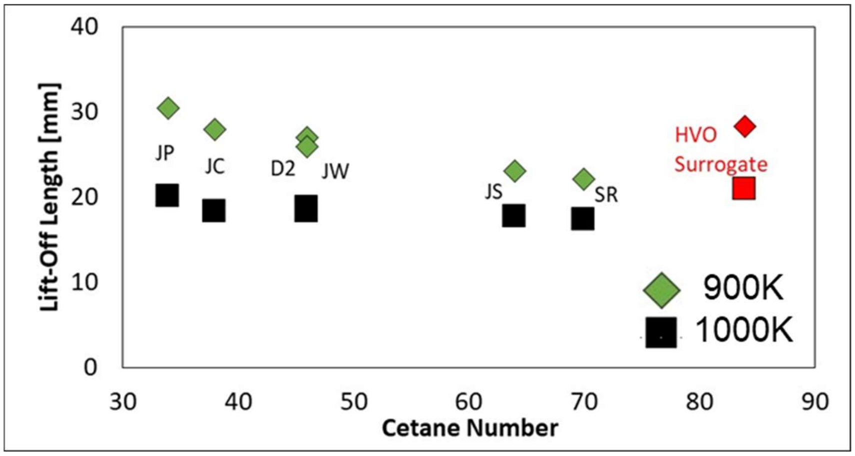

Fig. 3 – Lift-off Length

In this case the results are not in line with the decreasing trend: it has been shown in the previous sections that the lift-off length is a parameter that has to be investigated more and, however, is typically overestimated.

Ignition delay time results to be essentially dependant on the cetane number [35] and therefore on the fuel reactivity. The ambient temperature affects the ignition delay as well: it can be noticed, in fact, how the ignition delay spread reduces as the ambient temperature increases, resulting in having a high temperature sensitivity at low ambient temperature range.

Different authors have tried, in previous works, to propose a correlation between the lift-off length and the fuel characteristics: Pickett et al. [36], i.e., suggested that a shorter lift-off length was expected for fuels with shorter ignition delay time (and therefore, cetane number). This has been verified for different fuels and however some deviations were observed [37,28]. Payri et al. [38] investigated the lift-off length for two different Fischer-Tropsch fuels and observed that the one with lower boiling temperature presented a longer lift-off length: this suggests that the fuel evaporation has a significant effect on this characteristic. It can be hypothesized, then, that the cooling of the fuel/air mixture due to fuel evaporation results in a longer lift-off length. An first validation of this can be easily observed considering that HVO and conventional diesel (D2) present a similar liquid penetration and a similar lift-off length: in particular, the bio-fuel has a lower liquid penetration due to its lower boiling curve and, in fact, presents a slightly higher lift-off length with respect to diesel.

Moreover, these results and considerations are also in line with the recent work Bjørgen et al. [39] where the hydrotreated vegetable oil combustion has been investigated and compared to the one of traditional diesel and rapeseed methyl esters (RME, a FAME bio-diesel deriving from rapeseed oil).

The HVO analysis in reacting conditions has then been done to compare the apparent heat release rate (AHRR) with numerical results from diesel simulations.

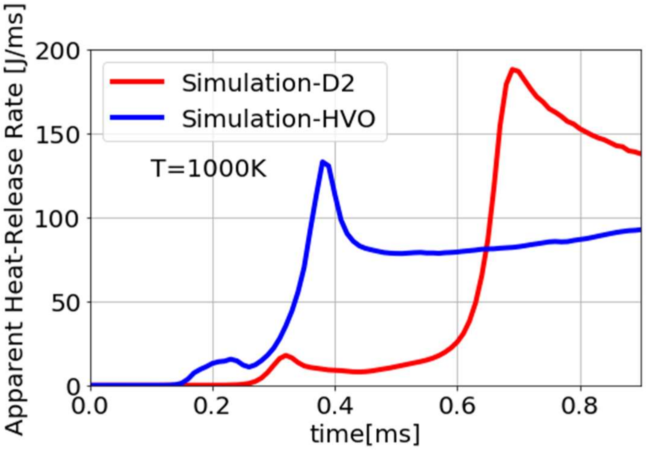

Fig. 4

In Fig.4 it can be observed that the HVO burns faster and with a lower peak than the traditional diesel: this is due to higher cetane number which results in shorter ignition delay and therefore a shorter premixed combustion phase. Moreover the presence of EGR, simulated considering an oxygen content of 15%, affects the rise of the heat release rate, smoothing it [40]. As the AHRR is calculated from the pressure rise, it can be noticed that using HVO as fuel will results in a smoother pressure rise, with probable effects on the engine noise as well. However it should be pointed out that the work of Ewphun et al. [41] shows that no significant differences have been found between the integral heat release from HVO and traditional diesel combustion: this suggests that the slower heat release could be negative in terms of NO_x emissions since the mixture is expected to stay at high temperature range for a longer period. This result is in line with those found in available literature [28].

Finally, the HVO has been compared to traditional diesel in terms of soot and NO_x emissions: this is reported in Fig.5a and Fig.5b respectively.

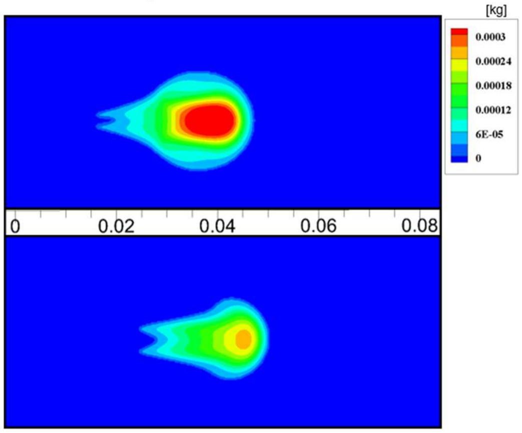

Fig. 5a – Hiroy Soot contours for Diesel (up) and HVO (low)

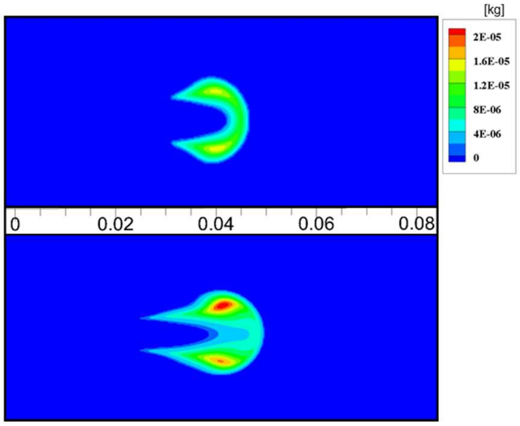

Fig. 5b – NO_x contours for Diesel (up) and HVO (low)

The delay between the start of the first ignition and soot formation is the time needed for the entrained air to be consumed during the premixed combustion: this increases the local temperature and results in a richer mixture consisting of fragmented fuel molecules, the ideal conditions for soot formation. Consequently HVO combustion results in lower soot formation with respect to diesel combustion, due to its lower ignition delay which results, as seen, in a shorter premixed combustion phase. Moreover the traditional diesel has a higher sooting tendency to its composition, with a significant content of cycloalkanes and aromatics, that produces more soot precursors. In Fig.5a this behaviour is presented and verified. The work of Bjørgen et al. [39] presents similar results, and points out that the oxygen content of FAME bio-diesels results in even lower soot formation.

The effect of using HVO, instead of traditional diesel, on NO_x formation should be positive since a reduced ignition delay thanks to the high cetane number results in a lower combustion temperature: the numerical simulations, however, produce a different result. This has to be investigated more in detail in future analysis, even though the work of Dimitriadis et al [42] points out that the variation of nitric oxide (NO_x) production is affected by different parameters such as the EGR percentage and the operating point of the engine.

6 CONCLUSIONS

6.1 Results discussion

Results show that the proposed approach to formulate a surrogate is suitable for its purpose, having a favourable trade-off between computational load and accuracy: the surrogates proposed and investigated are, in fact, able to mimic the spray and combustion characteristics of the target fuels. The only flaw in the presented approach is relative to the lift-off length: a deeper analysis of this characteristic is therefore strongly suggested. Moreover, the detailed kinetic mechanism can be further reduced to decrease the computational effort of the simulations. Attention must be paid to properly control the process so as to minimize the loss of accuracy. Moreover the calibration of the spray injection model can be improved in order to better simulate combustion characteristic like the lift-off length.

The HVO simulations have shown that apparently, this bio-fuel can be used instead of traditional diesel without performance losses due to limited liquid penetration (low risk of wall wetting) and a higher cetane number that results in a smoother AHRR. Moreover it has an advantage not only in terms of carbon dioxide emissions but also in terms of particulate matter emissions: however it should be remembered that in the performed numerical simulations, the hydrotreated vegetable oil produces more NO_x emissions. Therefore, a more detailed analysis on this behaviour has to be done. However the diesel engine still suffers the trade-off between these two emissions, no matter what type of fuel is adopted.

For sure, the analysis of hydrotreated vegetable oil is still at a beginning phase, but it has been shown that this new bio-fuel has high potentiality and an important role in reducing the carbon dioxide emissions.

6.2 Future steps of ENI project

To proceed with the ENI project it will be fundamental to perform a proper characterization of the fuels, with a particular focus on temperature dependant properties: this will allow to generate a surrogate fuel specific for the ENI traditional diesel and HVO and thus a higher accuracy in the 3D-CFD model. The CONVERGE CFD software, in facts, models the fuel injected by generating a liquid which can be user-defined with the following, temperature dependent, properties:

- Viscosity
- Surface tension
- Heat of vaporization
- Vapor pressure
- Thermal conductivity
- Density
- Specific heat

And the following, temperature independent, ones:

- Boiling and freezing temperatures
- Critical values (pressure, temperature, volume and compressibility)

Apart from the complete fuel characterization, which isn't necessary but it would be required to improve the method proposed in this thesis to an almost-state-of-the-art level, future steps to progress with this project will be the engine testing and the implementation of the surrogate approach and spray calibration, defined in this thesis, in the 3D-CFD engine model that is currently in phase of development with the research team of Prof. E. Spessa, Prof. M. Baratta, Prof. D.A. Misul and PhDs Student P. Goel.

Hopefully the completion of this project won’t be the ending of the study on biofuels, but will instead be the first step of many other research activities: moreover, the surrogate approach proposed in this work can be adjusted to simulate not only diesel-like fuels but also gasoline, allowing to investigate many more fuels.

References:

[1] Ayhan Demirbas, Biodiesel production from vegetable oils via catalytic and non-catalytic supercritical methanol transesterification methods, Progress in Energy and Combustion Science, Volume 31, Issues 5–6, 2005, Pages 466-487, ISSN 0360-1285

[2] Gvidas Š., Development of a 3D-CFD Model for the Analysis of Combustion and Emissions in a Light-Duty Diesel Engine

[3] Ferziger, J. H., Peric, M., Computational Methods for Fluid Dynamics, Springer, Berlin, 2002

[4] Anderson, J. D., Computational Fluid Dynamics. The Basics with Applications, McGraw-Hill, New York, 1995.

[5] Hoffmann, K. A., Chiang, S. T., Computational Fluid Dynamics. Volume I, Engineering Education System, Wichita, 2000.

[6] Moukalled, F., Mangani, L., Darwish, M., The Finite Volume Method in Computational Fluid Dynamics, Springer International Publishing, Switzerland, 2016.

[7] 24. CONVERGE Manual v2.4, Convergent Science, 2017.

[8] Company Profile, https://convergecfd.com/about/company-profile

[9] Issa, R. I., "Solution of the Implicitly Discretised Fluid Flow Equations by Operator-Splitting", Journal of Computational Physics 62, pp. 40-65, 1986.

[10] CONVERGE UDF Manual v2.4, Convergent Science, 2018.

[11] Senecal, P. K. et al., "Multi-Dimensional Modeling of Direct-Injection Diesel Spray Liquid Length and Flame Lift-off Length using CFD and Parallel Detailed Chemistry", SAE 2003-01-1043, 2003.

[12] Turns, S. R., An Introduction to Combustion: Concepts and Applications, McGraw-Hill, New York, 2012.

[13] Reitz, R. D., "Modeling Atomization Processes in High-Pressure Vaporizing Sprays", Atomisation and Spray Technology 3, pp. 309-337, 1987.

[14] Ren, Y., Li, X., "Assessment and validation of liquid breakup models for high-pressure dense diesel sprays", Frontiers in Energy 10(2), pp. 164-175, 2016.

[15] Reitz, R. D., Bracco, F. V., "Mechanisms of Breakup of Round Liquid Jets", Encyclopedia of Fluid Mechanics, Gulf Publishing Company, Houston, 1986.

[16] Kong, S. C., Han, Z., Reitz, R. D., "The Development and Application of a Diesel Ignition and Combustion Model for Multidimensional Engine Simulation", SAE 950278, 1995.

[17] Schmidt, D. P., Rutland, C. J., "A New Droplet Collision Algorithm", Journal of Computational Physics 164(1), pp. 62-80, 2000.

[18] Post, S. L., Abraham, J., "Modeling the Outcome of Drop-Drop Collisions in Diesel Sprays", International Journal of Multiphase Flow 28(6), pp. 997-1019, 2002.

[19] Ang Li, Lei Zhu, Yebing Mao, Jiaqi Zhai, Dong Han, Xingcai Lu, Zhen Huang, Surrogate formulation methodology for biodiesel based on chemical deconstruction in consideration of molecular structure and engine combustion factors, Combustion and Flame, Volume 199, 2019, Pages 152-167, ISSN 0010-2180

[20] C.L. Yaws, Yaws' Critical Property Data for Chemical Engineers and Chemists, 978-1-61344-932-5

[21] S.C. Kong, Y. Sun, R.D. Reitz, Journal of Engineering for Gas Turbine and Power 129 (2007) 245-251.

[22] P.K. Senecal, K.J. Richards, E. Pomraning, T. Yang, M.Z. Dai, R.M. McDavid, M.A. Patterson, S. Hou, T. Shethaji, SAE Paper (2007) 2007-01-0159.

[23] S. Som, S. "Development and Validation of Spray Models for Investigating Diesel Engine Combustion and Emissions;" PhD thesis, University of Illinois at Chicago; 2009.

[24]Som, Sibendu, Longman, Douglas, Luo, Zhaoyu, Plomer, M & Lu, Tianfeng. (2011). Three Dimensional Simulations of Diesel Sprays Using n- Dodecane as a Surrogate.

[25]Pitz, William & Mueller, Charles. (2011). Recent Progress in the Development of Diesel Surrogate Fuels. Progress in Energy and Combustion Science. 37. 330-350.

[26]C.J. Mueller, W.J. Cannella, T.J. Bruno, B. Bunting, H.D. Dettman, J.A. Franz, M.L. Huber, M. Natarajan, W.J. Pitz, M.A. Ratcliff, K. Wright, Methodology for Formulating Diesel Surrogate Fuels with Accurate Compositional, Ignition-Quality, and Volatility Characteristics, Energy & Fuels 2012 26 (6), 3284-3303

[27]Lin, R., & Tavlarides, L. L. (2012). Thermophysical properties needed for the development of the supercritical diesel combustion technology: Evaluation of diesel fuel surrogate models. Journal of Supercritical Fluids, 71, 136-146

[28]Kook, S. & Pickett, L. M. Soot Volume Fraction and Morphology of Conventional, Fischer-Tropsch, Coal-Derived, and Surrogate Fuel at Diesel Conditions. *SAE Int. J. Fuels Lubr.* **5**, 647–664 (2012).

[29]Lapuerta, M., Villajos, M., Agudelo, J. R. & Boehman, A. L. Key properties and blending strategies of hydrotreated vegetable oil as biofuel for diesel engines. *Fuel Process. Technol.* 92, 2406–2411 (2011).

[30]Pei, Yuanjiang & Mehl, Marco & Liu, Wei & Lu, Tianfeng & Pitz, William & Som, Sibendu. (2015). A Multi-Component Blend as a Diesel Fuel Surrogate for Compression Ignition Engine Applications (ICEF2014-5625). Journal of Engineering for Gas Turbines and Power. 137.

[31]Yachao Chang, Ming Jia, Yaopeng Li, Yaodong Liu, Maozhao Xie, Hu Wang, Rolf D. Reitz, Development of a skeletal mechanism for diesel surrogate fuel by using a decoupling methodology, Combustion and Flame, Volume 162, Issue 10, 2015, Pages 3785-3802, ISSN 0010-2180

[32]Dagaut, Philippe. (2002). On the kinetics of hydrocarbons oxidation from natural gas to kerosene and diesel fuel. Physical Chemistry Chemical Physics - PHYS CHEM CHEM PHYS. 4. 2079-2094.

[33]Siebers, D., "Liquid-Phase Fuel Penetration in Diesel Sprays," SAE Technical Paper 980809, 1998

[34]Company profile, https://ecn.sandia.gov/diesel-spray-combustion/experimental-diagnostics/

[35] Jung, S., Ishida, M., Yamamoto, S. et al. Enhancement of NOx-PM trade-off in a diesel engine adopting bio-ethanol and EGR. Int.J Automot. Technol. 11, 611–616 (2010)

[36]Pickett, L., Siebers, D., and Idicheria, C., "Relationship Between Ignition Processes and the Lift-Off Length of Diesel Fuel Jets," SAE Technical Paper 2005-01-3843,

[37]Manin, Julien & Skeen, Scott & Pickett, Lyle & Kurtz, Eric & Anderson, James. (2014). Effects of Oxygenated Fuels on Combustion and Soot Formation/Oxidation Processes. SAE International Journal of Fuels and Lubricants. 7.

[38]Payri, F., Pastor, J., Nerva, J., and Garcia-Oliver, J., "Lift-Off Length and KL Extinction Measurements of Biodiesel and Fischer-Tropsch Fuels under Quasi-Steady Diesel Engine Conditions," SAE Int. J. Engines 4(2):2278-2297, 2011

[39]Karl Oskar Pires Bjørgen, David Robert Emberson, Terese Løvås, Combustion and soot characteristics of hydrotreated vegetable oil compression-ignited spray flames, Fuel, Volume 266, 2020

[40]Yin, B., Wang, J., Yang, K. and Jia, H. (2014). Optimization of EGR and split injection strategy forlight vehicle diesel low temperature combustion. Int. J. Automotive Technology 15, 7, 1043−1051.

[41]Ewphun, P., Vo, C.T., Srichai, P. et al. Combustion characteristics of hydrotreated vegetable oil – diesel blend under EGR and supercharged conditions. Int.J Automot. Technol. 18, 643–652 (2017).

[42]Dimitriadis A, Natsios I, Dimaratos A, Katsaounis D, Samaras Z, Bezergianni S and Lehto K (2018) Evaluation of a Hydrotreated Vegetable Oil (HVO) and Effects on Emissions of a Passenger Car Diesel Engine. Front. Mech. Eng. 4:7.